Journal of Catalysis **209,** 365–384 (2002)
doi:10.1006/jcat.2002.3579

Steam Reforming and Graphite Formation on Ni Catalysts

H. S. Bengaard,* J. K. Nørskov,*,[2] J. Sehested,† B. S. Clausen,† L. P. Nielsen,†,[1]
A. M. Molenbroek,† and J. R. Rostrup-Nielsen†

*Center for Atomic-Scale Materials Physics, and Interdisciplinary Research Center for Catalysis, Department of Physics, Technical University of Denmark, DK-2800 Lyngby, Denmark; and †Haldor Topsøe A/S, Nymøllevej 55, DK-2800 Lyngby, Denmark

Received November 12, 2001; revised February 28, 2002; accepted February 28, 2002

Based on density functional theory calculations, kinetic measurements, microkinetic and Monte Carlo simulations, thermogravimetric analysis (TGA) experiments, extended X-ray absorption spectroscopy (EXAFS) measurements, and experimental results from the literature, we present a detailed and comprehensive mechanistic picture of the steam reforming process on a Ni catalyst. The complete potential energy diagram for the full reaction is presented and compared to experiments. Structures, energies of all reaction intermediates, and activation barriers are identified. We conclude that there are at least two kinds of active sites with different reactivities for steam reforming: a more active one associated with defect (step) sites, and a less active one associated with close-packed facets. It is further suggested that the nucleation of graphite is initiated at the step sites. We show that additives like potassium, sulfur, and gold preferentially bind to the step sites of Ni, and on this basis it is suggested that the promotion by these additives in terms of a higher tolerance toward graphite formation involves the same basic mechanism: blocking of the step sites.

1. INTRODUCTION

In the steam reforming process methane is dissociated on the surface of a catalyst, typically Ni based, molecular hydrogen is formed, and the remaining carbon is reacted with water to form additional molecular hydrogen and carbon monoxide (1). The process runs at high temperatures and most economically if the carbon-to-oxygen ratio in the feed gas is as close to stoichiometric as possible. However, under such conditions graphitic carbon can form, destroying the catalyst. Several ways of alleviating the problem of carbon formation have been suggested. The addition of alkali metal salts is known to reduce the problem considerably, but at the expense of a reduction of the reforming rate (2). Continuous addition of sulfur to the feed gas gives rise to a sulfur coverage on the surface which impedes carbon formation more than it reduces the reforming rate (3). Most recently it has also been found that the addition of slight amounts of gold to the catalyst increases the resistance toward graphite formation (4).

In the present paper we provide a new comprehensive picture of the steam reforming process, which can explain not only the known characteristics of the process itself but also the effect of various additives on the graphite formation process. Our analysis is based on a combination of new, detailed density functional theory (DFT) calculations, kinetic measurements, microkinetic simulations, and experimental investigations of the process in addition to a number of experimental results from the literature. We conclude that on a Ni catalyst there are at least two kinds of active sites for steam reforming (and of the reverse methanation process): one very active, associated with certain step and defect sites on the surface, and another less active, associated with the close-packed facets. The steps are suggested to be the nucleation sites for graphite formation, and it is further suggested that the different additives reducing graphite formation all work by blocking step sites.

In the following we start by summarizing the picture we have developed of the steam reforming process and the associated graphite formation. We do this to give an overview of the large number of calculations and experiments that we present in the rest of the paper. The methods used include density functional theory calculations of reaction mechanisms and energetics and of the bonding of alkali, sulfur, and gold promoters to a Ni surface. These calculations are complemented by detailed measurements and kinetic modeling of the methane activation rates on different Ni catalysts, by *in situ* measurements of the structure of additives on supported catalysts, by measurements of graphite formation in synthesis gas, and by previously published data for the steam reforming process.

2. OVERVIEW

Before going into a detailed discussion of our results and comparisons to previously published data, we briefly give an overview of the picture we have developed of the steam reforming process and associated graphite formation.

[1] Present address: NKT Research A/S, Technical University of Denmark, CAT, Build 347, DK-2800 Kgs. Lyngby.

[2] To whom correspondence should be addressed. E-mail: norskov@fysik.dtu.dk.

0021-9517/02 $35.00

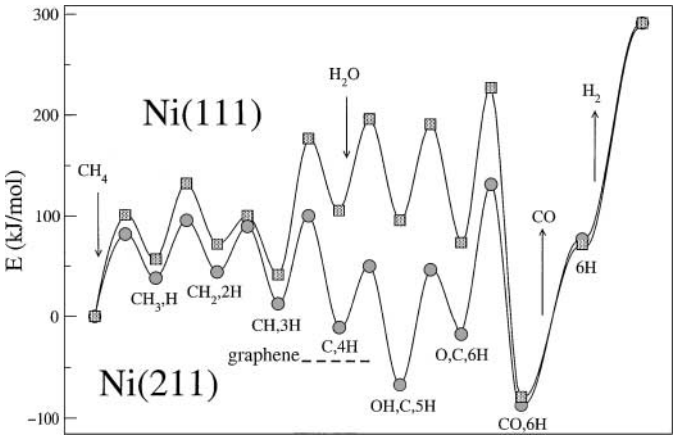

FIG. 1. Energies for the species on Ni(211) and Ni(111). All energies are relative to CH_4 and H_2O in the gas phase and calculated using the results for the individual species.

Figure 1 summarizes the results of our density functional theory (DFT) calculations of the steam reforming process over a Ni(111) surface and over a stepped Ni(211) surface. We note two important features:

1. The steps are more reactive than the close-packed surface for most of the elementary steps in the process, including the activation of methane, which is suggested to be among the rate-determining steps (5, 6).

2. Atomic carbon has much higher stability on steps than on terrace sites.

Point 1 indicates that there should be (at least) two different reaction channels: one with a low activation barrier which is associated with steps, and another associated with terraces. The latter channel has a higher barrier, and because there are more facet sites than step sites except for extremely small particles, it should have more surface sites available. Point 2 indicates that any nucleation of graphite on the surface of a Ni particle should start at steps. We note from Fig. 1 that graphene on Ni(111) is the most stable form of carbon on the surface, and that there is a driving force for graphene formation. It would therefore seem that the availability of step sites is important both for a large turnover rate and for graphite formation. This raises the question of where on the surface during turnover promoters such as alkali or sulfur are located.

We have used the DFT calculations to evaluate the stability of potassium, sulfur, and gold on Ni surfaces and find that both sulfur and gold are more stable at a step than on a terrace, and that potassium is more stable when it is bound to oxygen along the step. Likewise we find from the calculations that gold in the surface of Ni is attracted to step edges, and we show experimentally using EXAFS that this is indeed the case for Au/Ni catalysts. On this basis we suggest that the main graphite-preventing effect of these promoters is to block the steps and hence remove the nucleation sites for graphite formation.

We have made kinetic experiments of methane activation over Ni/spinel catalysts with and without potassium added and find two different reaction channels, one with a low barrier which is dominating for the potassium-free sample and another with a high barrier for the potassium-promoted sample. In light of the calculations we interpret this to mean that potassium blocks the more reactive step sites. This is supported by the finding that the preexponential factor for methane dissociation is 15 times higher over a potassium-promoted catalyst than over an unpromoted catalyst, indicating that many more sites are active in the former (terrace sites) than in the latter (step sites) catalyst. Additional support for this picture can be found in the literature, where it has been shown that the steam reforming activity can be correlated with the N_2 adsorption capacity of the catalyst. DFT calculations show that N_2 adsorption is quite strong at steps but weak at the (111) terraces of Ni. N_2 adsorption therefore titrates the most active sites in the steam reforming process.

In the following we first present the density functional calculational method used. In Section 4 the detailed results for the different elementary steps in the steam reforming process are presented. In Section 5 we discuss in detail the bonding of potassium and sulfur to different sites on Ni surfaces, and we give results for the most stable site for gold atoms in a nickel surface and supplement it with experimental data on the structure of Au/Ni catalysts. The reader not interested in these details can go to Section 6. Here we model in some detail the graphite nucleation process and show that a critical nucleus is needed for the process to proceed. In Section 7 we then go on to a discussion of the methane activation experiments and the kinetic modeling. Finally, we discuss the relation between the present findings and results from the literature. In particular we discuss here the possibility of using N_2 to titrate the step sites on a Ni catalyst.

3. STRUCTURAL MODELS AND CALCULATIONAL SETUP

For many systems the reactivity on stepped and defect sites is known to be very different from the reactivity found for the close-packed surfaces and steps may even determine the overall reactivity (7–9). Recently it was found that N_2 dissociation on the Ru(0001) surface is totally dominated by steps, with a measured adsorption rate at the step being at least nine orders of magnitude higher than on the terraces at 500 K (7). Direct observations using the scanning tunneling microscope revealed that the dissociation of NO preferentially takes place at steps on the Ru(0001) surface (8). The sticking probabilities for H_2 at the step sites of Si(001) surfaces were found to exceed those on the terraces by up to six orders of magnitude (9).

We have chosen the Ni(211) surface as a model to investigate the effect of steps. This surface consists of (111) facets

three atoms wide and separated by steps having the (100) geometry.

The theoretical part of this study is based on self-consistent density functional theory calculations, using the generalized gradient approximation (GGA) to describe exchange and correlation effects (10). The ionic cores are described by ultrasoft pseudopotentials and the RPBE (11) density is determined self-consistently by iterative diagonalization of the Kohn–Sham Hamiltonian, Fermi population ($k_BT = 0.1$ eV) of the Kohn–Sham states, and Pulay mixing of the electronic density (12). The RPBE functional is of the GGA form and is found to give a good description of molecular bond energies and of the chemisorption energetics of atoms and molecules on transition-metal surfaces (11, 13, 14). All energies have been extrapolated to $T = 0$. Plane waves with a kinetic energy cutoff of 25 Ry are used to expand the wave functions. The calculations are performed with the magnetic moment of the Ni surface taken into account.

The Ni surfaces were modeled by a periodically repeated supercell containing from three to five layers in the Ni(111) slab. A nine-layer slab of Ni was used in the Ni(211) calculations, giving a slab thickness that is comparable to the thickness of a (111) slab containing three layers. Two successive slabs were separated by a vacuum region of ~10 Å. For the results presented in Fig. 1, p(2 × 2) lateral unit cells were used to model the Ni(111) surface, with coverages of 25%, except for the activation of methane on Ni(111), where a p(3 × 3) lateral unit cell was used, and for the Ni(211) calculations (1 × 2) unit cells were used with a coverage of one adsorbate for each two Ni step edge atoms. Adsorption takes place at only one side of the slab with an appropriate adjustment of the electrostatic potential. The Brillouin zones were sampled at 16–18 special $\vec{k}$ points using the Monkhorst–Pack procedure for the Ni(211) slab and a Chadi–Cohen $\vec{k}$ point set for the Ni(111) slab to respect the symmetry of the system. For all the calculations a lattice constant $a = 3.52$ Å for bulk Ni was used. For the calculations on the isolated molecules H_2, H_2O, CO, N_2, and CH_4 we used a large supercell with a lattice constant of 10 Å. In addition, an increasingly negative binding energy of a species to the nickel surface means increasing the bond strength between the species and the surface.

3.1. Location of Transition States

We assume that the reaction coordinate consists primarily of the C–H bond stretch (C–O or H–O stretch for the dissociation of CO and water). We then fix the C–H (C–O, H–O) bond length and let the remaining degrees of freedom of the adsorbate and surface atoms relax. After several of these constrained optimizations with varying C–H (C–O, H–O) bond length we locate an approximate maximum in the energy as a function of the bond length. We check that the maximum in energy is associated with a change of sign of the slope of the forces. It should be noted that this simple approach is approximate. For the more complex reaction steps (CH_3 and CH_2 dehydrogenation on Ni(211), water activation on both surfaces) the nudged elastic band method (15, 16) has been employed.

4. THE REACTION MECHANISM

4.1. CH_x on Ni(111) and Ni(211)

The dehydrogenation of methane/hydrogenation of carbon and the chemisorption of CH_x ($x = 0, 1, 2, 3$) species on different transition metals have been studied extensively both experimentally and theoretically. Many theoretical studies on CH_4 and CH_x adsorption and dissociation focus on the close-packed surfaces of Ni (17–27) and other transition metals, such as Ru (28, 29), Pd (30, 31), and Ir (32).

Burghgraef *et al.* (17, 18) used DFT to study methane activation and dehydrogenation on Ni clusters. The barrier for CH_4 dissociation was found to be 121 kJ/mol for the largest (Ni_{13}) cluster used, whereas the overall reaction energies for the successive dissociation of the C–H bonds of methane were 30, 24, −27, and 27 kJ/mol, respectively.

Yang and Whitten (19, 20) reported results on the chemisorption of H and CH_x and the dissociative chemisorption of CH_4 on a Ni(111) surface using an embedded cluster CI approach. The calculated activation energy for CH_4 to produce CH_3 was 71 kJ/mol, and the reaction was predicted to be exothermic with 12 kJ/mol.

Siegbahn and Panas (21) investigated the chemisorption of CH_x fragments on the close-packed Ni(111) and Ni(100) surfaces and found similar stabilities on the two surfaces in cluster model calculations.

Kratzer *et al.* (22) performed DFT calculations on a Ni(111) slab with and without varying amounts of Au substituted into the surface layer to characterize the transition state for CH_4 dissociation. For the clean Ni surface the barrier was 109 kJ/mol, with the carbon atom located almost on top of a Ni atom.

Au *et al.* (23, 24) performed DFT calculations on model clusters to study the dissociation of methane on transition and coinage metals. For Ni the total dissociation of CH_4 to give $C* + 4H*$ was found to be exothermic by 0.77 kJ/mol on a Ni_7 cluster with the atoms distributed in the symmetry of the (111) plane.

Recently Michaelides and Hu (25, 26) investigated the adsorption of CH_2 and H and the dehydrogenation of CH_3 to form CH_2 on Ni(111) by means of DFT. They found an 48 kJ/mol endothermic reaction with a barrier of more than 100 kJ/mol and a C–H bond distance of 1.8 Å in the transition state.

Ciobîcă and coworkers (28, 29) studied the dissociation of CH_4 on the close-packed Ru(0001) surface. They investigated all the steps down to C + 4H on the surface and found barriers of 85, 49, 16, and 108 kJ/mol for the decomposition

of methane, methyl, methylene, and methylidyne, respectively. They found that the most stable species on the Ru(0001) surface was CH, and all of the surface species were found to prefer the threefold sites.

Watwe *et al.* (27) used density functional theory and periodic infinite slabs to model the adsorption and dissociation of CH_x species on the Ni(111) surface. They found that all the intermediates prefer the threefold sites, and the highest activation barrier was found for methylidyne dehydrogenation ($CH* \rightarrow C* + H*$). The least stable intermediate relative to CH_4 was found to be ($C* + 4H*$).

In experiments close-packed surfaces were often chosen for studies of methane activation/methanation and the interaction of CH_x fragments with Ni surfaces (33–38). Several experiments give activation energies for CH_4 dissociation from thermal experiments in the range 52–59 kJ/mol (33–35) for the (111), (100), and (110) surfaces. Larsen and Chorkendorff (36) showed in their molecular beam studies that it is the first excited vibrational state that makes the major contribution to the sticking under thermal conditions; but estimating a barrier height depends on the chosen value for the sticking coefficient. They estimated an activation energy of 70–90 kJ/mol for dissociative CH_4 chemisorption from the (state resolved) sticking curve with the lowest vibrational state. Lee *et al.* (37) reported that CH_4 dissociates to give CH_3 and H on the Ni(111) surface. Yang *et al.* (38) found that at temperatures above 150 K CH_3 dissociates into adsorbed CH. Above 250 K C–C bond formation was observed to give C_2H_2 which eventually polymerize at high coverages to give adsorbed benzene. The relative stabilities of the CH_x species was therefore determined to be $CH_3 < CH + 2H < 1/2C_2H_2 + 2H < 1/6C_6H_6 + H_2$.

The energies of the species for the most stable sites from this work are presented in Fig. 1. All energies are relative to CH_4 and H_2O in the gas phase.

It is seen that on the stepped surface the most stable CH_x ($x = 1, 2, 3$) intermediate is ($CH* + 3H*$), as on the Ni(111) surface. Atomic carbon is even more stabilized, so ($C* + 4H*$) is the most stable intermediate in the methane dissociation process. On the stepped surface breaking of the first and second CH bond are slightly endothermic processes, whereas the remaining CH bonds are broken exothermically in contrast to the results for the Ni(111) surface, where also the breaking of the methylidyne C–H bond was found to be endothermic. All the stable intermediates follow the same trend: the stability is higher at the stepped Ni(211) than at the Ni(111) close-packed surface.

Except for the activation of methane, we have used the geometries and stable sites for the CH_x species on Ni(111) reported by Watwe *et al.* (27) as starting points in calculations on Ni slabs consisting of three layers, with the top layer and the adsorbate fully relaxed. The extra degrees of freedom lead to additional stabilization of the adsorbed species compared to their work on fixed two-layer slabs, but the trends are unchanged and the differences in bond distances are marginal.

4.1.1. CH_4 activation on Ni(111). The effect of adding more layers and using a larger lateral unit cell for CH_4 dissociation on the Ni(111) surface was tested, and the result of 101 kJ/mol given in Fig. 1 for this point only is taken from a five-layer calculation with all the degrees of freedom for the top four layers relaxed and with a (3×3) lateral unit cell. It is found that the Ni atom where the dissociation is taking place is lifted up from the top surface layer with about 0.3 Å, accompanied by a decrease in barrier height of about 24 kJ/mol relative to the barrier height obtained from a calculation on the smaller unit cell with relaxation of only the top surface layer, giving a barrier height of 101 kJ/mol. The activation of methane is treated in detail elsewhere (39). A similar effect has recently been reported for CH_4 dissociation on an Ir(111) surface (32).

In order to compare this result with experimental observations, a zero-point correction should be performed. In their analysis of the real modes at the transition state, Kratzer *et al.* (22) found a zero-point correction to the calculated barrier height of approximately −10 kJ/mol. They treated the methane molecule as a dimer H–CH_3, and the internal modes of CH_3 were neglected. It was therefore speculated that softening of these modes at the transition state could give an additional (negative) contribution to the zero-point correction to the barrier height. In addition, the larger surface relaxations in the (3×3) lateral unit cell used in this work result in a lower activation energy and relatively large deformations of the surface. It has not been possible to do calculations for a larger cell, and we can therefore not exclude the possibility that convergence of the activation energy with respect to the size of the supercell is not reached. Our estimate for the barrier is therefore that it is less than 91 kJ/mol, in good agreement with the experimental value of 70–90 kJ/mol (36). Later, in Table 5, we present an activation energy of 87 kJ/mol obtained by fitting experimental data with a microkinetic model. We have also calculated the barrier height using the PW91 (10) functional to describe the exchange-correlation energy. We find an activation energy of 70 kJ/mol with this expression. This value should then be subject to the zero-point correction, leading to an even lower barrier. This shows that the RPBE functional gives a better description.

Frequencies of the vibrational modes used in the calculations of the zero-point energies and heat capacities at constant pressure are listed in Table 1.

4.1.2. CH_3 on Ni(211). The most stable site for methyl adsorption is on top of an edge atom with one C–H bond perpendicular to the step edge direction. The C–H bond distances are all 1.10 Å, and the C–Ni distance is 1.94 Å.

4.1.3. CH_2 on Ni(211). We have investigated the adsorption of CH_2 at the fivefold coordinated step site and

TABLE 1

Frequencies of the Vibrational Modes Used in the Calculations of the Zero-Point Energies (ZPE) and Heat Capacities at Constant Pressure

	ν (cm^{-1})[a]	ZPE (kJ/mol)	C_p (kJ/mol)[b]
CH_4	2916.7	113	35.31
	1533.6		
	3018.9		
	1306.2		
H_2O	3656.7	54	33.58
	1594.8		
	3755.8		
CO	2169.8233	13	29.12
H_2	4400.39	26	28.82

[a] From Ref. (57).
[b] From Ref. (58).

at the step edge. We find that CH_2 prefers adsorption at a bridge site at the step edge in a configuration where the CH_2 fragment is perpendicular to the step edge. Putting CH_2 in a parallel configuration with respect to the step edge leads to relaxation toward the perpendicular configuration. The C–H bond lengths are 1.10 Å.

4.1.4. CH on Ni(211). We find that CH is most stable when bonded to the fivefold coordinated site at the step. We also tested the threefold site at the (111) terrace that is nearest to the step edge. The C–H bond distance is 1.11 Å.

4.1.5. Carbon on Ni(211). Carbon adsorbs strongly to the fivefold coordinated site at the step with a distance of only 1.81 Å to the nearest Ni atom. We also calculated carbon on Ni(211) at the double coverage of one C to one Ni edge atom. For this coverage carbon is less stable by 43 kJ/mol.

4.1.6. Hydrogen on Ni(211). Hydrogen is found to bind at the bridge site at the step on Ni(211) with a vertical distance of 1.05 Å to the topmost Ni layer at the step. Adsorptions at the fivefold coordinated site at the step and different threefold sites at the (111) terrace all had higher energies than the bridge site.

4.2. CO on Ni(211) and Ni(111)

We calculated the barrier for dissociation of CO on the two surfaces and found a large structure dependency. CO binds with 176 (188) kJ/mol on Ni(111) (Ni(211)) and the barrier for dissociation is 299 (201) kJ/mol. CO was found to prefer the threefold site on the planar (111) surface. The step is more reactive than the (111) facet for CO dissociation, whereas for the reverse reaction of carbon and oxygen association the barriers at the two surfaces are of the same magnitude, as seen in Fig. 1. The CO bond distances are 1.18 and 1.20 Å when adsorbed on Ni(211) and Ni(111), respectively.

A large number of investigations are concerned with the CO adsorption energy on Ni(111) (see, e.g., (40), and references therein, where the adsorption energy estimate is 125–130 kJ/mol, based on intensive studies of the literature, and with experiments giving values between 108–150 kJ/mol and theory giving energies between 144–193 kJ/mol). It has been found that in general CO adsorbs dissociatively on the transition metals listed in the upper left corner of the periodic table and molecularly on the transition metals list in the lower right corner. Ni is close to the border separating the transition metals so the structure of the surface is expected to affect the adsorption behavior of CO (41). Usually CO is adsorbed molecularly at temperatures below 300 K on the low-index nickel surfaces, followed by CO desorption when the temperature is increased to about 450 K and no carbon or oxygen is left on the surface. For stepped or sputter-damaged surfaces CO dissociation has been reported. Nakano *et al.* (42) studied the carbon deposition from CO on a Ni(977) surface and suggested that CO dissociates at the step edges. Also Erley and Wagner (43) found that the step edges on a Ni(977) surface (5(111) × (110)) easily dissociated adsorbed CO in a thermal flash desorption experiment. Experiments on a sputter-damaged Ni(100) surface gave a high CO dissociation probability of 0.4 (44), compared to reaction probabilities between 10^{-4} and 10^{-2} on the low-index Ni(100) and Ni(110) surfaces (45, 46). The sticking coefficients on both the annealed and the sputter-damaged surfaces were found to be independent of beam energy, and it was suggested that also on the annealed surface the mechanism is surface migration to defect sites followed by dissociation. Nakano found a negative activation energy for CO dissociation on Ni(977) (adsorption energy of CO is larger than the dissociation barrier of CO^{ads}). A negative activation energy was also reported by Astaldi *et al.* (46) on a sputter-damaged Ni(100) surface.

Altogether these experimental results indicate that CO dissociation (and carbon formation) take place at the step or defect sites supporting the picture from the theoretical analysis presented here.

4.3. Water on Ni(111) and Ni(211)

Experimentally, Ni surfaces are found to have very varying degrees of reactivity toward water, ranging from relatively unreactive close-packed (111) and (100) surfaces, where water is adsorbed reversibly, to the more open (110) surface and stepped surfaces, where water can either chemisorb without clustering or dissociate, depending on the conditions (47–50). In the dissociation of water defects like steps and kinks are believed to be important in the initiation (47–49). In an experimental study of the interaction of water with the stepped Ni(760) surface (7(110) × (100)) by Kasza *et al.* (47) a much higher reactivity toward dissociation was found compared to the Ni(110) surface. Benndorf

and Mundt (48–50) investigated stepped Ni surfaces with terraces having the (111) orientation and found states from thermal desorption spectras that had not been observed on the planar Ni(111) surface. The states were attributed to H_2O adsorbed molecularly at step sites and to the recombination of water dissociation products. When increasing amounts of Na were coadsorbed with H_2O on the stepped Ni surface the step states and the terrace state disappeared until only a Na-induced state remained. The disappearance of the step states was explained by a preferred adsorption of Na atoms at the steps (50). Similar results on water adsorption have been reported for stepped Ru surfaces, where new desorption states with higher desorption temperatures, which are absent on the flat Ru(0001) surface, were observed (51).

DFT calculations on water adsorption on the two surfaces showed that water is only very weakly bonded, with −2 and −1 kJ/mol at the Ni(211) and Ni(111) surfaces, respectively. We expect that at high water coverage the formation of a hydrogen bonding network will be important and this could explain the differences between experiment and the calculations presented here. The O...Ni bond distances are in both cases quite long, about 3.0 Å.

The barriers for the reaction

$$H_2O* + * \rightleftharpoons OH* + H*$$

were calculated to be 91 kJ/mol for Ni(111) and 38 kJ/mol for Ni(211) (cf. Fig. 1). This agrees nicely with the experimental observations. The barrier at the (111) facet is too large for dissociation at room temperature while at the step the water dissociation can take place.

4.4. OH on Ni(211) and Ni(111)

On the planar Ni(111) surface the calculated O–H distance was found to be 0.977 Å, and the distance from the first Ni layer to O was 1.38 Å, with oxygen adsorbed in the fcc threefold hollow site. We also tested the top site for adsorption but it was significantly less stable. Similar results from DFT cluster calculations have been reported by Koper and van Santen (52), who found that in general hydroxyl adsorption is about 1 eV stronger in the hollow site on the (111) surface relative to the on-top site, and by Yang and Whitten (53), who also found preference for adsorption at the threefold site on Ni(111) using an ab initio CI theory approach. On the stepped Ni(211) surface the OH group prefers bonding at the bridge site of the step edge with 0.983 Å between O and H. We also tested adsorption at the fivefold coordinated site at the step but the energy was higher. The most stable state at the Ni(211) surface was 70 kJ/mol more stable than the most stable state at the planar Ni(111) surface.

The barriers for the reaction

$$OH* + * \rightleftharpoons O* + H*$$

were determined (cf. Fig. 1). For the planar Ni(111) surface the barrier was 96 kJ/mol and for Ni(211) the barrier was 114 kJ/mol, or 18 kJ/mol *higher* on the stepped than on the planar surface. The transition state is still considerably lower in energy at the step than on the (111) surface, and water dissociation will be much more effective at the step.

4.5. Oxygen on Ni(211) and Ni(111)

Adsorption of atomic oxygen on the Ni(111) surface is found to take place at the fcc hollow site, with the hcp site for adsorption being less stable. The distance from oxygen to the nearest Ni neighbor was 1.86 Å, which corresponds to a perpendicular distance of the oxygen atoms from the first Ni layer of 1.15 Å. Experimentally it was found in an NEXAFS study that adsorption of oxygen occurs at the threefold-coordinated fcc site both in the p(2 × 2) (0.25 ML) and in the $(\sqrt{3} \times \sqrt{3})R30^\circ$ (0.33 ML) superstructures with a nearest-neighbor O–Ni bond length of 1.85 ± 0.05 Å (54), whereas electron-energy-loss fine-structure spectroscopic investigations using a heavily oxidized sample gave a distance of 1.94 ± 0.05 Å for the (2 × 2) structure (55).

At the (211) surface we calculated adsorption of oxygen to be most stable when oxygen is bonded to the threefold site closest to the step, whereas bridge bonding to the step edge atoms and adsorption at the fivefold site both were less stable.

Energetically, the bonding of oxygen is found to be the same on the two surfaces. In a study on oxygen adsorption and coadsorption with CO on the stepped Ni(775) surface Kirstein *et al.* (56) found that the CO adsorption sites at the steps vanish first with increasing oxygen precoverage and it was concluded that oxygen adsorption starts at the steps.

4.6. The Overall Reaction

For the overall steam reforming reaction of methane,

$$CH_4 + H_2O \rightleftharpoons CO + 3H_2,$$

$\Delta H^{\theta}_{298} = 206$ kJ/mol. For our calculations presented here we get $\Delta E = 292$ kJ/mol, as illustrated by the final point in Fig. 1. In order to compare this number with the experimentally determined ΔH^{θ}_{298}, we have to include zero-point energies and to correct for the variation of the enthalpy of reaction with temperature, $\Delta C_p \Delta T$, where ΔC_p is the change in heat capacity at constant pressure for the reaction, and it is assumed to be independent of the temperature. Using the data in Table 1 we get an estimated $\Delta H^{\text{theory}}_{298} = 230$ kJ/mol, in reasonable agreement with the experimental value.

5. THE STRUCTURE OF ADDITIVES

In the following we present results from DFT calculations on the structure of the additives potassium, sulfur, and gold on Ni surfaces. The calculations are supported

by experimental results from extended X-ray absorption fine-structure spectroscopy (EXFS) experiments on Au/Ni catalysts and Monte Carlo simulations.

5.1. Alkali Adsorption

Alkali compounds are used as catalyst promoters for many important reactions, and the effect on the chemisorption of molecules on alkali metal precovered transition metals has been studied for a number of systems (59). For the steam reforming process, tests by Rostrup-Nielsen and Christiansen of a series of Ni and other transition metal catalysts with and without potassium (or Li or Na) added showed that the activation energy for methane dissociation remained almost constant whereas the rate per unit metal surface area strongly decreased with increased potassium loading (60).

For the methane/Ni system Ceyer *et al.* (61) found no effect of potassium on the dissociation probability of methane and therefore expected no effect on the rate of steam reforming from potassium deposition. This is in contrast to another report that shows that the addition of alkali to the nickel catalyst may lower the reaction rate by more than one order of magnitude (1) and also in contrast to a combined adsorption and DFT study on the chemisorption of methane on Ni(111) and Ni(100) surfaces where the methane sticking probability was shown to be strongly diminished by the presence of potassium in the coverage range 0–0.12 monolayer (62).

5.1.1. Potassium adsorption on Ni(211) and Ni(111). We calculated the adsorption of potassium on the two surfaces. On the (111) surface the atop site for adsorption is slightly preferred over the threefold site in the p(2 × 2)-K lateral unit cell, with a binding energy of −126 kJ/mol. The atop site in the p(2 × 2)-K unit cell has also been found experimentally using angle-resolved photoemission extended fine structure, photoelectron diffraction, and LEED (63–65), with K–Ni bond distances of 3.02 ± 0.01, 2.86 ± 0.03, and 2.82 ± 0.04 Å, respectively. We found a K–Ni bond length of 2.83 Å. Adsorbed in the $(\sqrt{3} \times \sqrt{3})$R30°, p(4 × 2), and $(2 \times 2\sqrt{3})$ structures potassium is less stable compared to the p(2 × 2)-K structure.

For the stepped surface we tested three sites, on top of an edge atom, a bridge site at the step edge, and the fivefold coordinated site at the step, with the latter being the most stable, with a binding energy of −138 kJ/mol. This means that bonding at the step is favored, with 12 kJ/mol over bonding at the (111) facet.

At the working temperature of the real catalyst for steam reforming (800–1300 K) the alkali adlayer will not be stable and the alkali atoms will therefore desorb.

5.1.2. Bonding of K on an O-precovered surface. The coadsorption of oxygen is known to stabilize an alkali adlayer (66, 67). In general the coadsorption of oxygen with alkali metals on nickel leads to structures where the oxygen bonds to the substrate and the alkali atoms are located either in the same layer or in a layer above the oxygen. Ordered overlayers consisting of O and alkali can form at appropriate coverages (68).

Li and Diehl (69) used LEED to study the coadsorption phases of oxygen and potassium on Ni(111) and proposed a phase diagram for K + O/Ni(111). For oxygen coverages between 0.1 and 0.25 ML they found a p(2 × 2) phase when K is coadsorbed, and this phase transformed into a $(\sqrt{3} \times \sqrt{3})$R30° phase via a region of coexistence of the two phases with increasing coverage of potassium. The structure of the $(\sqrt{3} \times \sqrt{3})$R30° overlayer structure was not reported, but a preferred K : O stoichiometry was not observed, suggesting that the $(\sqrt{3} \times \sqrt{3})$R30° phase may not be a cooperative structure between K and O but might be due to oxygen ordering on its own, with the potassium randomly distributed and only giving rise to diffuse background in the LEED experiment. For higher oxygen coverages the deposition of potassium leads to a c(4 × 2) phase; the detailed structure is not known. It is well-known that on the Ni(100) surface at certain conditions a (3 × 3) phase exists where K and O are coadsorbed and form a cooperative structure where both the oxygen atoms and the K atoms participate in the ordering (70–72).

We calculated structures of coadsorbed K and O on the Ni(111) surface and along the stepped Ni(211) surface to see if oxygen on these surfaces would be able to give extra stability to the adsorbed potassium. We had to restrict ourselves to phases with translational symmetry and a size of the unit cell suitable for the periodic DFT calculational setup. For the 1 : 1 K : O stoichiometry we tested the p(2 × 2) ($\theta_K = \theta_O = 0.25$ ML) and the $(\sqrt{3} \times \sqrt{3})$R30° ($\theta_K = \theta_O = 0.33$ ML) lateral unit cells on the Ni(111) surface and also a p(4 × 2) chainlike structure with $\theta_K = \theta_O = 0.125$ ML. We also tested a 2 : 1 K : O ratio with a K coverage of $\theta_K = 0.25$ ML on the Ni(111) surface in a rectangular $(2 \times 2\sqrt{3})$ supercell. The different stoichiometry did not have a strong influence on the adsorption of K on the (111) surface. The structures are shown in Fig. 2. The results for bonding of potassium on the Ni surfaces with and without a precovering of oxygen are summarized in Table 2 for the structures with the strongest bonding of potassium. It is seen that when potassium is adsorbed on an O-precovered surface of Ni(111) the binding energy per K atom changes by 5 kJ/mol relative to the clean Ni(111) surface, whereas potassium adsorbed on the oxygen-precovered Ni(211) surface is more stable by 62 kJ/mol relative to the clean surface. The largest stabilizing effect of oxygen is found at the step.

5.1.3. Support for K adsorption at step: N_2 adsorption. Early work (2) indicated that the strong decrease in activity for steam reforming and hydrogenolysis by the addition of alkali was accompanied by the disappearance of special

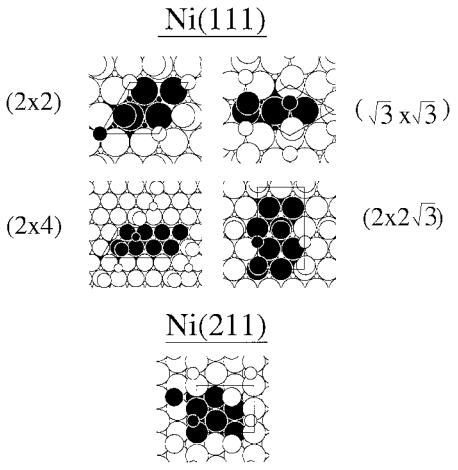

FIG. 2. The KO coadsorption structures investigated. The super cells used are indicated, with the smallest spheres being oxygen and the darkest being potassium.

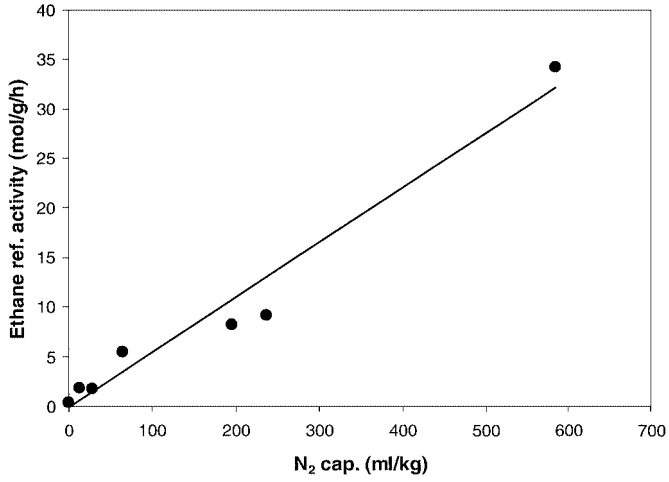

FIG. 3. Rate of steam reforming of ethane (773 K) vs nitrogen capacity for a series of alumina-supported nickel catalysts (2).

(B_5) sites on the nickel surface. These sites were determined by adsorption of nitrogen at room temperature using the method suggested by Van Hardeveld and coworkers in a series of papers (73–75) for the determination of B_5 sites. Several authors (76–79) challenged the method for determination of B_5 sites. However, Arumainayagam *et al.* (80) and Tripa *et al.* (81) recently showed that adsorption of N_2 on Pt is restricted to step defect sites. Adsorption of N_2 on Ni(111) is observed at low temperatures. Quick *et al.* (78) and Yoshinobu *et al.* (79) studied adsorption of nitrogen on Ni(111) at temperatures of 83 and 89–115 K, respectively. Extrapolation of the adsorption isotherms of nitrogen reported by Yoshinobu *et al.* to room temperature shows that N_2 does not adsorb on Ni(111) at room temperature and N_2 pressures below 1 bar. It therefore seems reasonable to conclude that the adsorption of N_2 on nickel catalysts at room temperature only takes place at step defect or B_5 sites, as proposed by Van Hardeveld and co-workers.

Rostrup-Nielsen (2) studied the effect of potassium promotion on the N_2 adsorption capacity and some results are given for alumina based catalysts in Table 3 and in Fig. 3. It is evident from Table 3 that potassium promotion of catalyst C3 does not change the surface area of the active phase and the total BET (Brunauer, Emmett, and Teller) area. However, potassium has a strong effect on the N_2 adsorption capacity, suggesting that the number of step defect sites is strongly reduced by potassium. In Fig. 3, the activity for ethane reforming is plotted as a function of the N_2 capacity for a series of alumina-supported Ni catalysts (2). A good correlation exists between the activity and the N_2 capacity for both potassium-promoted and nonpromoted samples. The correlation is not good between the activity and the nickel surface area when the potassium-containing samples are included. We therefore propose that potassium preferentially sticks to the highly uncoordinated nickel atoms at the step defect sites and that these largely determine the activity of the nickel catalyst. This conclusion supports the DFT calculations above, which showed that potassium only bonds strongly to step defect sites and is therefore not displaced by N_2. Calculations of the binding energies of N_2 to Ni(111) and Ni(211) are performed in the following section.

TABLE 2

Binding Energies (kJ/mol) for Potassium on the Ni Surfaces without or Precovered with Oxygen and the Corresponding Differences in Energies between Adsorption at the Clean and the Oxygen-Precovered Surfaces

	Ni(111) (p(2 × 2))	Ni(211) (p(2 × 2))
E/K (kJ/mol)	−126	−138
E/(K/O@Ni) (kJ/mol)	−131	−206
Δ (kJ/mol)	−5	−68

5.1.4. DFT calculations on N_2 adsorption. Calculations of the binding energy of N_2 at Ni(211) and Ni(111) were performed. For end-on adsorption on Ni(111) the bridge, fcc, hcp, and atop configuration were examined with the atop configuration being the most stable with a binding energy of −8 kJ/mol. The other configurations that were examined for Ni(111) did not show a stabilization of N_2. Experiments suggest that N_2 on Ni is adsorbed at atop sites normal to the surface (78, 82).

On the stepped Ni(211) surface the bridge and atop adsorption sites of the step edge were examined. The most stable state found was the atop molecular state where N_2 is adsorbed end-on on top of a step edge atom binding with −49 kJ/mol.

The calculated stable states on the two surfaces are similar to what has previously been found for N_2 adsorption on Pt(112) and Pt(111) surfaces in a theoretical and

TABLE 3

Key Data for Ni/Al_2O_3 Catalysts[a]

Name	Support	Comment	Ni (wt%)	Ni area (m^2/g)	BET area (m^2/g)	N_2 capacity (ml/kg)	Act. C_2H_6, 773 K (mol g^{-1} s^{-1})
C3	γ-Al_2O_3		20	3.62	71.1	196	0.82
C10	γ-Al_2O_3	C3 + 2.1% K	20	4.19	76.4	13	0.19

[a] C3 and C10 obtained from Table 5-3 in Rostrup-Nielsen (2). C10 is prepared by addition of potassium to catalyst C3.

experimental study (81). In their study Tripa *et al.* presented DFT calculations on the binding of N_2 to Pt(111) and Pt(112), which showed that N_2 only binds to the step with a difference in adsorption energy of 49 kJ/mol between the most favorable state on Pt(112) and the most favorable on Pt(111). They also found experimentally that the saturation coverage of N_2 on Pt(779) is half of that on Pt(335), and this is the same as the ratio of the number of step defect sites on the two facets. The calculations presented here for Ni surfaces show that N_2 is preferentially bonded to the step edge favored with 41 kJ/mol over bonding at the planar (111) surface.

It is interesting to note that while Van Hardeveld and coworkers (73–75) used N_2 adsorption to identify high-coordination (B_5) sites, N_2 actually prefers to be one-coordinated. However, a step site consists of both a high- and a one-coordinated site, and therefore the N_2 adsorption capacity can be used to titrate the step sites.

5.2. Sulfur Adsorption

Several chemisorbed phases of sulfur on Ni(111) have been reported (83). The dissociative chemisorption of H_2S at room temperature leads to several structures, depending on the coverage. First a p(2 × 2) phase ($\Theta_S = 0.25$ ML) is produced, followed by the $(\sqrt{3} \times \sqrt{3})$R30°-S phase ($\Theta_S = 0.33$ ML). For these two phases S atoms occupy the fcc hollow sites and the phases are believed to be "simple" sulfur overlayers with one sulfur atom per unit mesh on an almost undistorted Ni(111) surface (84). The structure of Ni(111)-p(2 × 2)-S has been determined with several different experimental techniques, including low-energy electron diffraction (LEED), surface extended X-ray absorption fine structure (SEXAFS), photoemission, and ion scattering (84–87).

At higher coverages a deformation of the $(\sqrt{3} \times \sqrt{3})$R30°-S phase ($\theta_S = 0.41$–$0.48$ ML (83, 88)) takes place. At higher temperatures or from postannealing of the mentioned phases more complex phases ($(\sqrt{39} \times \sqrt{39})$ (88) and various rectangular phases) are formed. For these complex phases extensive reconstruction of the Ni substrate has been proposed (89). In a study of the $(\sqrt{39} \times \sqrt{39})$ ($\theta_S = 0.22$ ML) phase between 675 and 1175 K STM data give direct evidence both of a preferential formation of the $(\sqrt{39} \times \sqrt{39})$ phase at substrate monatomic steps and that nucleation takes place preferentially at step edges. This indicates that the sulfur atoms that diffuse on the surface at these elevated temperatures are trapped at the step sites. After nucleation the growth was found to proceed on both the upper and the lower terraces on Ni(111) (90).

5.2.1. DFT calculations on S adsorption on Ni surfaces. We calculated the adsorption structure and energetics of S on the two Ni surfaces. For the Ni(111) surface we chose the p(2 × 2)-S unit cell and calculated both the fcc and the hcp sites on four-layer-thick Ni slabs, allowing the two topmost layers and the sulfur atom to fully relax. The most stable site was the fcc site with a distance of 1.59 Å to the Ni surface, in good agreement with experimental data from X-ray standing wavefield absorption (84) and low-energy ion scattering in the impact collision mode (ICISS) (91). For the Ni(211) surface a (1 × 2) unit cell was chosen. Here we tested two different sites for adsorption, a threefold site next to the step and the site at the step where S is five-coordinated, with the latter being more stable. The results for the most stable sites on the two surfaces show that sulfur bonding is favored at the step with 37 kJ/mol over bonding at the (111) facet.

5.2.2. The influence of S adsorption on C formation. The adsorption of sulfur and the influence of sulfur adsorption on the rate of reforming and carbon formation were studied in detail by Rostrup-Nielsen (3). Rostrup-Nielsen determined the rate of methane reforming at 1123 K for $\theta_S = 0.7$–0.83 and the rate of carbon formation for $\theta_S = 0.77$–0.82. At these sulfur coverages the rate of methane reforming (r_{ref}) and the rate of carbon formation (r_C) was proportional to $(1 - \theta_S)^{-2.7}$ or $(pH_2S/pH_2)^{-0.8}$ and $(1 - \theta_S)^{-6.3}$ or $(pH_2S/pH_2)^{-1.9}$, respectively. The stronger dependence on $(1 - \theta_S)$ of r_C than of r_{ref} was proposed to be a consequence of the larger number of active sites needed for carbon formation than for methane reforming. This suggestion elegantly explains the experimental data. However, the DFT calculations presented above offer an alternative explanation of the data given by Rostrup-Nielsen (3). The difference in the binding energy of sulfur to step and to terrace sites gives rise to a lower coverage of sulfur at the latter sites. The calculations strongly support the idea that carbon only nucleates at step sites and hence the rate of carbon

formation will decrease strongly with an increasing sulfur coverage. However, at the high temperature, 1123 K, used by Rostrup-Nielsen, the rate of reforming may be controlled by terrace sites. This assumption is supported in two ways: (i) using the difference in the adsorption energy of sulfur to step and to terrace sites results in a two orders of magnitude difference in the equilibrium constant for adsorption of sulfur, assuming an equal entropy of adsorption at the two sites; and (ii) the kinetic measurements of methane activation presented in the following suggest that the rate of the first methane dehydrogenation reaction at a terrace site is only 2.5 times lower than at step sites at 1123 K. It could therefore be that terrace sites dominate the rate of reforming at the conditions used by Rostrup-Nielsen (3). In that case the lower coverage of sulfur at these sites compared to step sites is expected to lead to a slower dependence of the rate of reforming compared to that of the rate of carbon formation on the pH_2S/pH_2 ratio.

It is not possible with the present knowledge to judge between the interpretations of the data given by Rostrup-Nielsen (3) and that given here. However, it is important to note that the mechanism suggested by Rostrup-Nielsen is not in variance with the work presented here because the calculations do not decide whether carbon formation involves more sites than reforming.

5.3. Gold Adsorption

5.3.1. DFT calculations. To see to what extent gold is attracted to the step edge of a Ni particle we performed two calculations on a nine-layer Au/Ni(211) slab with the top three layers, including Au, fully relaxed. In one setup one Ni atom sitting along the step edge was replaced with a gold atom and in the other setup a Ni atom in the middle of the (111) microfacet of the (211) surface was replaced by an Au atom, as illustrated in Fig. 4. The calculations showed that gold at the step edge is favored with 36 kJ/mol over gold in the (111) facet.

5.3.2. EXAFS and Monte Carlo simulations. The atomic structure and the surface segregation of Au on Ni nanoparticles were simulated using the effective medium theory in a Monte Carlo scheme. A series of statistically independent snapshots of nanoparticles obtained after equilibration was used as input for EXAFS calculations. The resulting Fourier transformed EXAFS spectra are compared directly to EXAFS data obtained from *in situ* measurements on supported Ni/Au steam-reforming catalysts.

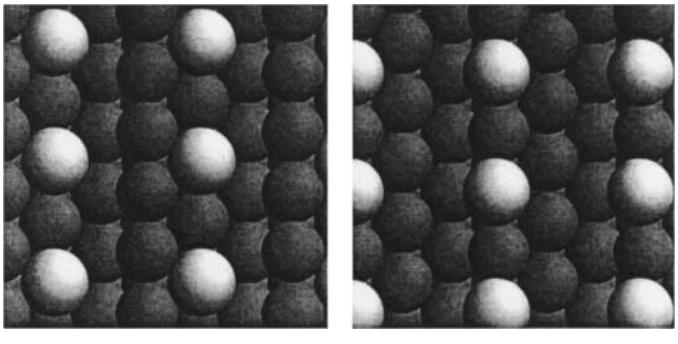

FIG. 4. A Ni atom (light) substituted by a Au atom at the (111) facet (left) and at the step edge of the Ni(211) surface.

5.3.3. Monte Carlo simulations on Au/Ni nanoparticles. The effective medium theory (EMT) (92) was used to describe the interatomic potentials in nanometer-size Au/Ni clusters. Monte Carlo simulations using the ArtWork code (93) and the EMT potentials for Au and Ni were performed on Au/Ni alloy clusters. The simulations were performed as described previously (94, 95): A spherically truncated fcc crystallite, with Au and Ni atoms placed randomly at lattice sites, was chosen as a starting configuration for the simulations. Only low Au/Ni atomic ratios are considered in the remainder (up to 4 at%), so the initial lattice constant of the cluster was chosen as the Ni lattice constant. Simulations were performed at two different temperatures: 300 and 1200 K. The first temperature was chosen to compare simulations to experimental results obtained at room temperature, and the next one to get results close to the industrial steam reforming temperature. The largest diameter of the cluster chosen for these simulations was 35 Å (2123 atoms). The Monte Carlo scheme allowed for two types of trial moves. The first one swapped the labels of two atoms, which mimics segregation of the alloy. The second one allows for the total volume of the cluster to be changed isotropically. Equilibration of the clusters typically takes place within a few hundred Monte Carlo cycles, in which the size of the cluster was changed and an attempt was made to swap the labels of all atoms in the cluster. Figure 5 shows an example of the result of a Monte Carlo simulation for a Au/Ni catalyst particle which consists of 2123 atoms, with a Au/Ni atomic ratio of 2%, equilibrated at 1200 K. Similar results were obtained for smaller particles and lower temperatures. Both at 300 and at 1200 K, the Au atoms are located at surface positions of the Ni nanoparticle. In addition it is clear that the Au atoms preferentially move to low-coordination sites. Even at high temperatures, no Au atoms were observed in the bulk of the particle. Furthermore, the Au atoms do not show a tendency to form clusters on the Ni particle and are roughly evenly spread.

5.3.4. EXAFS measurements and calculations. EXAFS spectra at the Ni K- and the Au L_3-edge were collected on silica and spinel-supported Ni and Au/Ni catalysts in the as-prepared state, after reduction, and after steam reforming in diluted *n*-butane. The results were published previously (95). Here, we only consider EXAFS spectra obtained at the Au L_3-edge, as data at this edge are sensitive to alloy formation only (for low Au concentrations). The circles in Fig. 6 show the Fourier transformed XAFS spectrum for a spinel-supported Au/Ni (1.7 wt% Au, 9.6 wt% Ni on $MgAl_2O_4$;

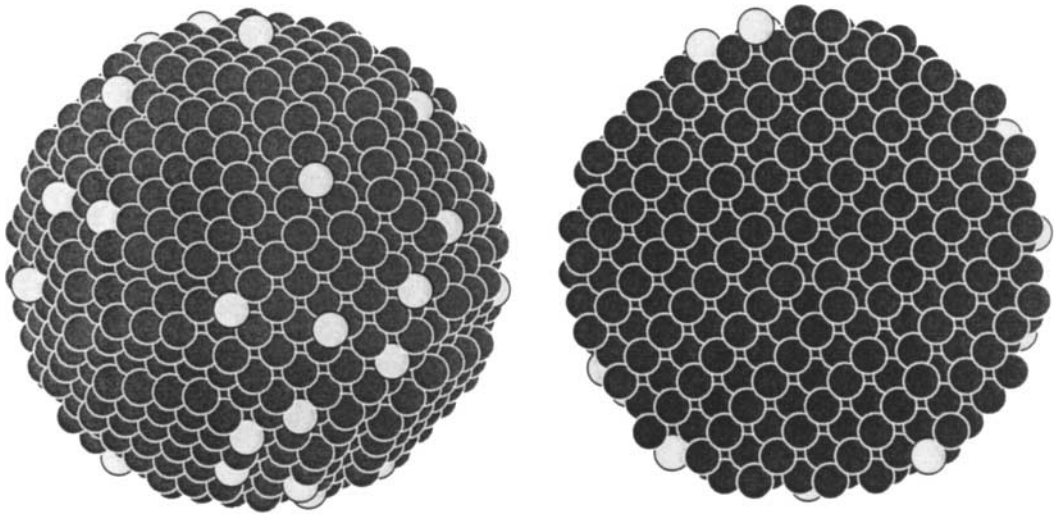

FIG. 5. Snapshot of a Au/Ni nanoparticle after equilibration in a MC scheme at 1200 K. The particle consists of 42 Au atoms (light) and 2081 Ni atoms (dark) with an outer diameter of 35 Å. (Left) Projected snapshot of the Au/Ni particle, with Au present as a surface alloy at the surface of the Ni cluster. (Right) Snapshot sliced through the center of the particle.

atomic ratio, Au/Ni = 0.053) catalyst after reduction in hydrogen.

The Fourier transformed data obtained from the measurements are compared directly to calculated XAFS data. The EXAFS calculations were performed on model Au/Ni systems using the FEFF 8.00 code to compute the absorption spectra (96, 97). Results from code tests on bulk Au and Ni were published previously (95) and showed that calculated and measured data are in good agreement. Input parameters for the calculations were thus chosen identical to those described in (95).

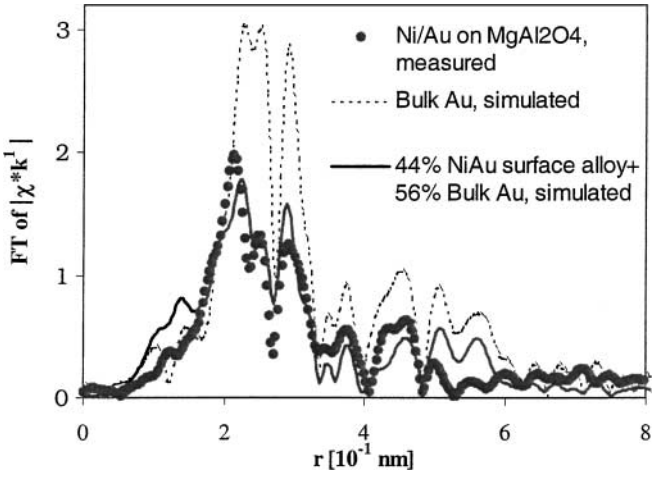

FIG. 6. Magnitude of the Fourier transformed EXAFS spectra at the Au L_3-edge at room temperature. The circles show measured data on a spinel-supported Au/Ni catalyst after reduction at 823 K in hydrogen. The dashed curve is the result of a calculated bulk Au spectrum. The full curve is the best fit to the measured data using a linear combination of 44% of the Au present in a Au/Ni surface alloy (with Au/Ni = 0.04 on spherically truncated Ni particles with a diameter of 2 nm) and the remainder of the Au present as large, bulklike Au particles.

The dashed curve in Fig. 6 shows the Fourier transformed spectrum obtained from a calculation of bulk Au. Clearly this curve does not mimic the data. A direct comparison between measured and calculated data is difficult because of the large fraction of pure Au particles present in most of the samples. A linear combination of calculated spectra of a Au/Ni surface alloy and bulk Au was chosen to mimic the experimental data. The spectrum for the surface alloy was calculated using the average of a series of spectra obtained from 10 statistically independent equilibrium snapshots of a 20-Å particle (369 atoms in total) with a Au/Ni atomic ratio of 0.038. Thermal vibrations were calculated by means of the Debye model using bulk Debye temperatures (Θ_{Au} = 185 K). The measured data was subsequently fitted using a linear combination of the averaged surface-alloy spectrum and the calculated spectrum of bulk Au (dashed curve in Fig. 6). The best fit (full curve in Fig. 6) resulted in 44% of the total amount of Au being present as a surface alloy. The remainder of the Au is supposed to be present in separate large Au particles (with an average coordination number close to 12).

Effects of particle size distribution, possibly adsorbed gasses, and interactions with the substrate were not included in the calculations.

Altogether this supports the conclusion that potassium, sulfur, and gold preferentially stick to the highly uncoordinated nickel atoms at the Ni step sites. This indicates that the main graphite-preventing effect of the additives could be the ability to suppress the access for carbon to the step/defect sites. In the following we model the graphite nucleation process using the results from the DFT calculations.

6. GRAPHENE ISLAND FORMATION ON Ni(111)

The structure and energy of the carbon formed in a catalyst usually deviates from ideal graphite. Several types of carbon formation, including so-called encapsulating carbon, pyrolytic carbon, and carbon whiskers, consisting of long filaments of carbon have been reported. Only the two latter types of carbon lead to deactivation of the catalyst. The type of carbon formed depends on the feed stock, temperature, and $H_2O : C_xH_y$ ratio. The carbon structure of the filament is graphene formed into tubes, with a diameter close to the diameter of the nickel particle (1).

The growth mechanism of the carbon filament is not fully understood. A commonly accepted mechanism consists of (i) decomposition of the carbon-containing gas on the surface of the metal particle, (ii) the isolated carbon atoms then dissolving into the bulk, and (iii) diffusing to facets that are suitable for filament growth (facets at the support side of the metal particle). The steady state growth is maintained by a constant diffusion of carbon atoms through the Ni particle (1, 98–100). The distribution of carbon atoms then gives rise to a concentration gradient: the surface of the front of the particle is enriched with carbon atoms. Below this selvage the carbon concentration decreases over a number of atomic Ni layers to the bulk concentration of dissolved carbon. It has been proposed that the carbon solubility at the front side (Ni/gas interface) is different from that at the Ni/filament interface (101), and this concentration gradient could be the driving force for the bulk diffusion of carbon through the Ni particles. The rate for filament formation is believed to be determined by this diffusion process through the bulk Ni particles. It has been observed that carbon formation has an initiation period. Within this model it could be explained as the time it takes to saturate the Ni particle with carbon.

6.1. The Graphene Overlayer

A graphene layer on Ni(111) lies commensurate to the surface. The bulk lattice constant of graphite is 2.46 Å; so by forming the overlayer on Ni a slight expansion is necessary to match the Ni substrate.

Experimental structure determination by Rosei *et al.* (45) on the (graphene overlayer)/Ni(111) system using extended energy-loss fine-structure spectroscopy gave a model with two types of carbon at threefold hollow sites: one located at an fcc site and one at an hcp site. Gamo *et al.* (102) investigated the graphene overlayer by means of low-energy electron diffraction spectroscopy. A structural model with one carbon atom located at the on-top site of the topmost Ni atoms and another carbon atom at the fcc hollow site gave the best fit.

We calculated the stabilization of graphene on Ni(111) using the two mentioned models. A four-layer slab was used where the two upper layers of Ni and the carbon atoms were allowed to fully relax. The model with the carbon atoms in the threefold hollow sites was slightly preferred, with 2 kJ/mol over the on-top/fcc hollow site model.

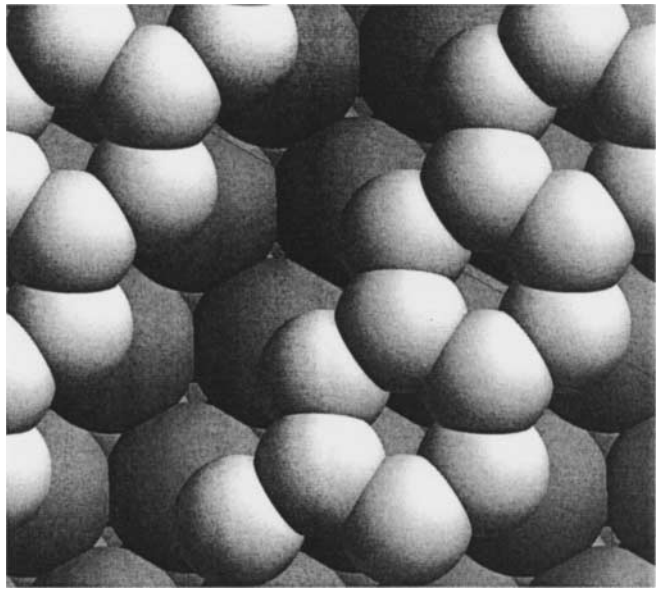

FIG. 7. Structure used for calculation of the edge energy of the graphene edge. Half the carbon atoms (light) are edge atoms; the rest of the carbon atoms have three carbon neighbors, as in the infinite graphene overlayer.

To get an estimate for the edge energy of the graphene edge of the island we performed DFT calculations on the structure shown in Fig. 7. Half the carbon atoms of this structure have the coordination of the infinite graphene overlayer with three neighboring carbon atoms, and the other half of the carbon atoms are undercoordinated edge atoms in the zigzag configuration. The coverage of carbon was four atoms (two bulklike, two edgelike) to three Ni atoms in the lateral unit cell (2C : 1Ni for the graphene overlayer). For this calculation a four-layer slab with the two topmost Ni layers and the carbon atoms fully relaxed was chosen. The edge energy was calculated as

$$E_{\text{edge}} = \frac{E(\text{C, Ni}) - E(\text{Ni}) - 4E_{\text{graphene}}}{2},$$

where E(C, Ni) is the total energy of the graphene edge calculation, E(Ni) is the total energy of the clean Ni surface, and E_{graphene} is the energy of a carbon atom from the calculation on the graphene-covered surface. In the calculational setup we had two carbon edge atoms in the supercell and for the edge energy per C atom we then find $E_{\text{edge}} =$ 172 kJ/mol.

In their DFT study on carbon nanotubes Lee *et al.* (103) calculated the edge energy for a carbon nanotube and found values of 212 and 289 kJ/mol per carbon edge atom, depending on the termination of the nanotube. In their calculations on nanotubes there is of course no interaction between the

TABLE 4

Relative Energies (kJ/mol) per Carbon Atom on the Two Surfaces, and the Edge Energy for Graphene on Ni(111)

	Ni(211) atomic C		Ni(111)		
	1C : 2Ni edge atoms	1C : 1Ni edge atom	Atomic C	Monolayer graphene	Graphene edge energy
E (kJ/mol)	0	43	97	−33	172

unpaired electrons at the edge and a substrate, so this leads to the much higher edge energies. When the graphene layer is at the Ni surface the unpaired electrons of the edge carbon atoms attempt to establish bonds with the underlying Ni neighbors. In the calculations presented here we find for the relaxed geometry of the carbon string that it showed deviations from the planar graphene hexagons. The C edge atoms are 0.27 Å closer to the surface than the C atoms that are surrounded by three C neighbors. This stabilizes the edge, and the edge energy per C atom in the graphene overlayer is lower than the values for the carbon nanotube.

Comparing the stabilization of a carbon atom the relative energies per C are given in Table 4. For carbon the most stable form is therefore the graphene overlayer on Ni(111), 33 kJ/mol more stable than that adsorbed at the step and the least stable atomic carbon on Ni(111).

6.2. *Critical Graphene Island Size*

For Ru surfaces steps are suggested to play a central role in the formation of graphitic overlayers (104). In an STM and HREELS study of the graphitic overlayers formed from the decomposition of CH_4 on Ru surfaces Wu *et al.* found that on the planar Ru(0001) surface at 800 K the graphite growth is two dimensional, with carbon islands consisting of many small clusters, ∼10–15 Å in diameter. These islands adsorb on the step edges and cover part of the lower lying terraces. Only at higher temperatures do the small carbon clusters coalesce to form a superstructure commensurate with the underlying Ru(0001) surface. They suggested a mechanism for the formation of these graphite clusters where CH_4 decomposes to form atomic carbon and then the initial nucleation of carbon atoms occurs preferentially at the edge sites of the Ru surface. The formation of graphite on the much more open Ru(11$\bar{2}$0) surface which has a variety of different adsorption sites was found to be very different from the Ru(0001) surface. At the (11$\bar{2}$0) surface large three-dimensional particles of graphite form from CH_4 at 800 K. It should be noted here that Ru does not form whisker carbon.

In a study of graphite formation from decomposition of CO on Ni(111) thin films it was found that films that were highly stepped and oriented approximately 3–5° from the (111) pole were highly active for graphite deposition, in contrast to the relatively inactive Ni(111) bulk single crystal. This observation could be due to both the increased rate of CO dissociation as well as the increased stability of carbon at stepped surfaces (105).

The stability of a graphene island on Ni(111) is determined by two contributions to the total energy: the relative low edge energy and the energy gain of forming the bulk graphene overlayer. When the graphene island formation sets in, the number of C edge atoms is relatively high compared to the number of atoms in the bulk of the graphene island. This means that in the beginning the cluster is unstable. At a certain critical cluster size the cost of forming the edge is balanced by the gain of forming the island, and for clusters larger than the critical cluster size the stability increases with the number of atoms in the island.

We have used the results from the DFT calculations to estimate the critical cluster size. We set the zero of energy to carbon adsorbed at the Ni(211) step. This means that carbon in the graphene monolayer on Ni(111) has the energy $E_{\text{graphene}} = -33$ kJ/mol according to the results given in Table 4. The calculations show that atomic carbon is stabilized at the step. The step could therefore act as nucleation site for graphite formation. We use a model where the shape of the graphene cluster is semihexagonal and bonded to the step, as shown in Fig. 8. The island contains N_{tot} atoms in total, and of these N_{edge} are edge atoms. The total energy of the cluster is therefore given as

$$E = N_{\text{tot}} \times E_{\text{graphene}} + N_{\text{edge}} \times E_{\text{edge}},$$

where $E_{\text{edge}} = 172$ kJ/mol. Using the chosen form of the graphene island and the calculated energies, the total energy of the island first rises as the number of atoms in the

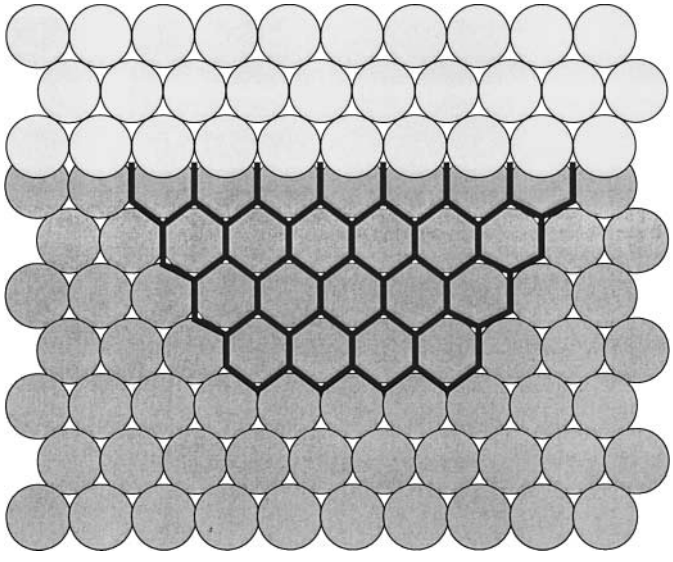

FIG. 8. The graphene island used in the model is semihexagonal and attached to a step edge.

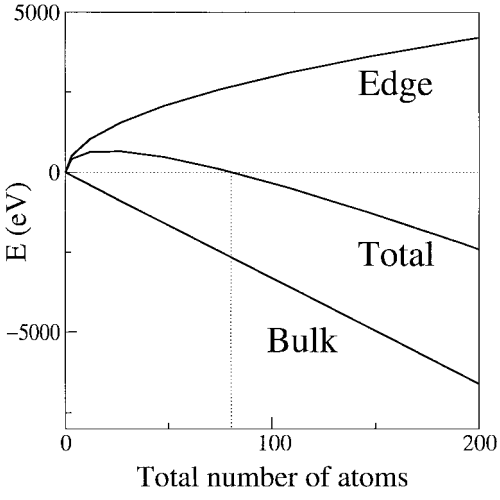

FIG. 9. The total energy of the island, the edge energy, and the bulk energy as a function of the number of atoms in the island.

cluster is increased, then goes through a maximum, and then decreases with the number of atoms. At a point the total energy becomes zero. Increasing the number of atoms in the cluster from this critical island size just leads to increased stability of the island. This is illustrated in Fig. 9, where the total energy, the edge energy, and the graphene bulk energy are shown as a function of the total number of atoms in the graphene cluster. With this simple model we get a critical cluster size $N_{\text{tot}}^{c} \sim 80$ atoms. This means that the side of the island that is bonded to the step is ~25 Å long when the shape of the cluster is semihexagonal, as shown in Fig. 8. This indicates that particles with facets smaller than this should not be able to nucleate graphite islands.

Experimental observations of weight of carbon versus process time (1, 2, 99, 106) show a certain initiation period with increasing rate of carbon formation before the coking rate reaches a constant (steady state) value. The necessary critical cluster size estimated in this work may explain the initiation period as the time required to assemble the quite large number of atoms needed to reach stability of the graphene island.

6.3. *Formation of the Carbon Whisker*

It is not the objective of this work to give the full picture of the formation of carbon on nickel, but a few comments regarding the formation of a carbon whisker from a critical graphene cluster are made. When a critical cluster is formed, the carbon cluster can grow by making a step around the nickel particle and covering part of the particle with a graphene layer. At high temperatures, single graphene planes may grow out from the particle forming a nanotube. At lower temperatures there is not sufficient energy for this process to proceed and, hence, a carbon whisker is formed. For whisker growth it is required that one layer of carbon be lifted from the Ni(111) planes present at the interface between the particle and the carbon whisker. However, the interface between the nickel particle and carbon whisker cannot be Ni(111) only and steps must be present both at the edge of the nickel particle–carbon whisker interface and away from the edge. It is likely that formation of a new layer of graphene for the carbon whisker is initiated from these step sites, where carbon atoms are stabilized relative to carbon at terrace sites. Hence, step sites may also be important for the growth of carbon whiskers.

6.3.1. Particle size and carbon formation. In order to elucidate the impact of the Ni crystallite size on the rate of carbon formation we performed TGA measurements. Rostrup-Nielsen (2) showed that the nickel particle size has a pronounced effect on the CH_4/H_2 ratio in the gas over the catalyst pellet at the point of equilibrium where carbon is neither formed nor removed from the catalyst. It has also been reported in the literature (see, for example, Borowiecki (107)) that the nickel particle size changes the rate of carbon formation and the limit of coking in synthesis gas. However, the interpretation of these studies is difficult due to different temperatures of catalyst pellets with different activities and the possible effect of film diffusion in the TGA unit. These problems can be overcome by careful preparation of catalysts with different mean nickel particle sizes but similar nickel surface areas and activities. Here we prepared two catalysts, containing 15 and 0.92 wt% nickel supported on a $MgAl_2O_4$ carrier with a BET area of 15 m^2/g. The catalysts were reduced in hydrogen gas at 798 K for 4 h before use. X-ray diffraction showed nickel and $MgAl_2O_3$ spinel as the only phases after reduction. The activity of the catalysts were determined to be 0.29 and 0.26 mol/g/h at 773 K in a mixture containing 19% CH_4, 7% H_2, and 74% H_2O. The active nickel areas of the catalysts were determined by sulfur chemisorption according to Rostrup-Nielsen (2) to be 0.90 and 1.00 m^2/g. From these numbers and the nickel loadings we calculate mean particle sizes of 1020 and 70 Å, respectively. The fact that the two catalysts have essentially the same activity and the same pore system (the same carrier was used) ensures that the temperature of the catalyst pellets and film diffusion around the two pellets will be similar.

The data for the active surface area and the methane reforming activity given above show that the activity per active surface area is within the uncertainty equal in spite of the 15-fold difference in crystallite size. This is apparently in variance with the data presented here, which indicate that steam reforming takes place at step sites, since small regular particles have more step defect sites than larger ones (74). However, only very few numbers of Ni atoms lead to regular Ni particles and Ni atoms will therefore be present on the particle surface to form steps. Entropy will be a large driving force for the formation of a large number of step defect sites while energy considerations will tend

to minimize the number of these sites. Strongly adsorbing molecules may even form their own steps on the particle surface. It is beyond the scope of this paper to go into a detailed discussion on this subject; we rather want to point out that there is good reason to believe that large metal particles will have a large number of step defect sites on their surface.

The TGA experiments were conducted in a rebuild CAHN microbalance setup interfaced with a gasfeed system and two H_2O bobble containers in series held at 308 and 292 K, respectively. The dual H_2O system was necessary in order to obtain a stable H_2O partial pressure of 21.4 mbar. Prior to the carbon experiments the prereduced catalysts were reduced *in situ* in 100 N ml/min hydrogen (N60) from room temperature to 798 K (6.5 K/min), where the temperature was held for 1 h. Subsequently the catalyst was cooled in the hydrogen flow to 573 K. At 573 K the flow was switched through the H_2O containers and after 10 min the gas mixture was changed to a premixed carbon-containing gas bottle (7% H_2/3% *n*-Butane/90% He), 76.4 N ml/min, which was mixed with He (N60), 217.15 N ml/min, to obtain a total flow of 300 N ml/min with an O/C ratio of 0.7. After 3 h at 573 K the temperature was raised to 873 K (0.5 K/min).

Figure 10 shows the relative weight increase as a function of the temperature for the two catalysts with an O/C ratio of 0.7. From the figure, it is clear that the onset temperature for the growth of carbon is approximately 100 K higher for the catalyst with 70-Å nickel particles than for that with 1020-Å nickel particles. Furthermore, the rate of carbon formation is much smaller for the smaller Ni crystallites. It is evident that a lowering of the nickel crystallite size increases the initial temperature of carbon formation. It therefore seems reasonable to assume that the low rate of carbon formation

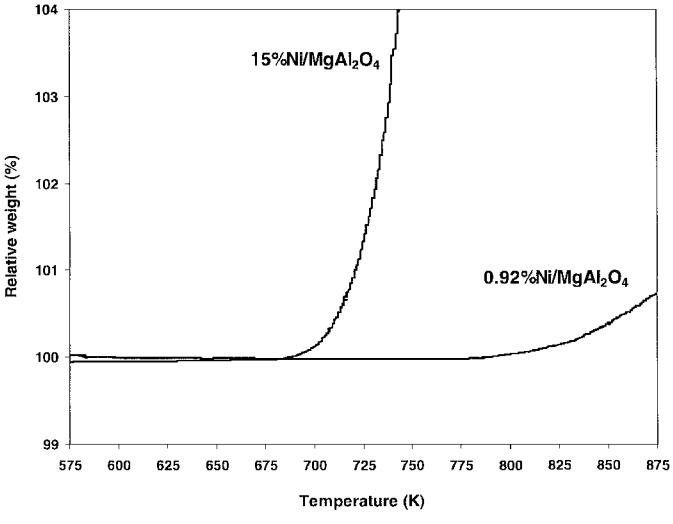

FIG. 10. Relative weight increase as a function of temperature for two Ni catalysts containing 15 and 0.92% Ni and similar nickel area using an O/C ratio of 0.7. See text for details.

observed for the catalyst with small nickel particles occurs at least partly because only a small fraction of the small Ni crystallites form carbon at the conditions used. This is in line with the DFT calculations, which suggest that small nickel particles do not form carbon.

7. EXPERIMENTAL METHANE ACTIVATION AND KINETIC MODELING

We now present further experimental results supporting our hypothesis that alkali metals block step sites on Ni catalyst particles.

7.1. Experimental

7.1.1. Catalysts. The activity for methane activation was measured for two catalysts. Both catalysts contained 14 wt% Ni and were supported on a $MgAl_2O_4$ carrier. Catalyst 1 contained no potassium while catalyst 2 was promoted with 1.2 wt% potassium. The nickel surface areas were determined by H_2S chemisorption as described in (1). The metal surface areas were calculated to be 4.7 and 4.0 m^2/g for catalyst 1 and 2, respectively, with a monolayer of sulfur equaling 44×10^{-9} g of S/cm^2 (1). The number of surface nickel atoms was calculated from the metal surface areas and an average site area for nickel of 6.5 $Å^2$ as estimated by (1). Premixed gases were purchased from commercial suppliers. Their purity was checked by mass spectrometry.

7.1.2. Experimental setup. The experimental apparatus is described in detail elsewhere (5) and is only described briefly here. The setup permitted the establishment of two parallel flows, one with pure hydrogen and one with 5% CH_4 in D_2. One of the gas flows went through a bypass and one went through the reactor system. The reactor effluent was monitored with a mass spectrometer. In all the experiments, the gas flows through the reactor system and the bypass were both set at 50 ml/min at NTP (pressure = 101.325 kPa, temperature = 0°C) conditions, and the total pressure in the system was set to 1.4 bar.

A recirculating reactor system rather than a single-pass reactor was used because a gas phase with no concentration gradients was desired. The recirculation pump delivered a recirculation flow rate of ca. 6 l/min (NTP), sufficient to maintain well-mixed conditions. That simplified the computer simulation of the results and the extraction of rate constants from the data. The catalyst zone consisted of a removable U-shaped glass-lined stainless steel tube in which 0.2 g of catalyst was held between wads of quartz wool. The tube had an inner diameter of 4.0 mm, which gave a catalyst bed height of 15–20 mm. The catalyst temperature was determined by a thermocouple inside the reactor resting on top of the catalyst bed. Catalyst particles in the size range from 0.3 to 0.5 mm were used.

The reduction and the measurement of the activity for methane activation were carried out as follows. First, the

catalyst was heated in hydrogen to 798 K and was reduced at this temperature for 4 h. Then the temperature was decreased to 673 K and 5% CH_4 in D_2 was allowed into the reactor. The mass spectrometer signals were stable after ca. 10 min. The activity was determined after 20 min at 673 K. Then the temperature was changed and after 20 min a new measurement could be performed.

7.1.3. Computer simulations. The rate of methane activation was measured using a gas mixture of 5% CH_4 in D_2. In this gas mixture the following reaction could be studied:

$$CH_4 \xrightarrow{D_2} CH_xD_{4-x}.$$

Mass spectrometer detection and microkinetic simulations of this reaction established microkinetic parameters for methane dehydrogenation on the catalyst surface. To extract rate constants from the experimental data the results from a computer model were fitted to the experimental results with the program "CATALYST II" (108). This program accepts as input a series of elementary reactions, their rate constants, and a description of the reaction conditions and proceeds to calculate gas-phase and surface concentrations by solving the mass balances of all reactants, products, and surface intermediates.

7.2. Kinetics of the Methane Activation Process

7.2.1. Measurements. The steady state concentrations of CH_4, CH_3D, CH_2D_2, CHD_3, and CD_4 as determined by the spectrometer signals at mass 16–20 are plotted in Figs. 11 and 12 for the $Ni/MgAl_2O_4$ and the $K/Ni/MgAl_2O_4$ catalyst, respectively. The data in Figs. 11 and 12 show that the reaction between CH_4 and D_2 begins at temperatures of 548 K ($Ni/MgAl_2O_4$) and 623 K ($K/Ni/MgAl_2O_4$). The reaction mixture is equilibrated at a temperature of 748 and 823 K for $Ni/MgAl_2O_4$ and $K/Ni/MgAl_2O_4$, respectively. It is evident that potassium promotion reduces the activity dramatically. In the following section the concentrations of CH_4, CH_3D, CH_2D_2, CHD_3, and CD_4 as a function of temperature are simulated using microkinetic modeling to obtain rate constants for the dehydrogenation of methane on the catalytic surface.

7.2.2. Microkinetic modeling. For the two nickel catalysts, the observed steady state concentrations versus temperature for all five methane isotopomers could be satisfactorily described by the following microkinetic model:

$$CX_4 + 2* \rightleftharpoons CX_3* + X* \quad k_1, k_{-1} \qquad [1]$$

$$CX_3* + * \rightleftharpoons CX_2* + X* \qquad [2]$$

k_2

$$k_{-2} = 2 \times 10^{12} \left(\frac{\text{molec}}{\text{site} \cdot \text{s}}\right) \exp\left(\frac{-77.5\ \text{kJ/mol}}{\text{RT}}\right),$$

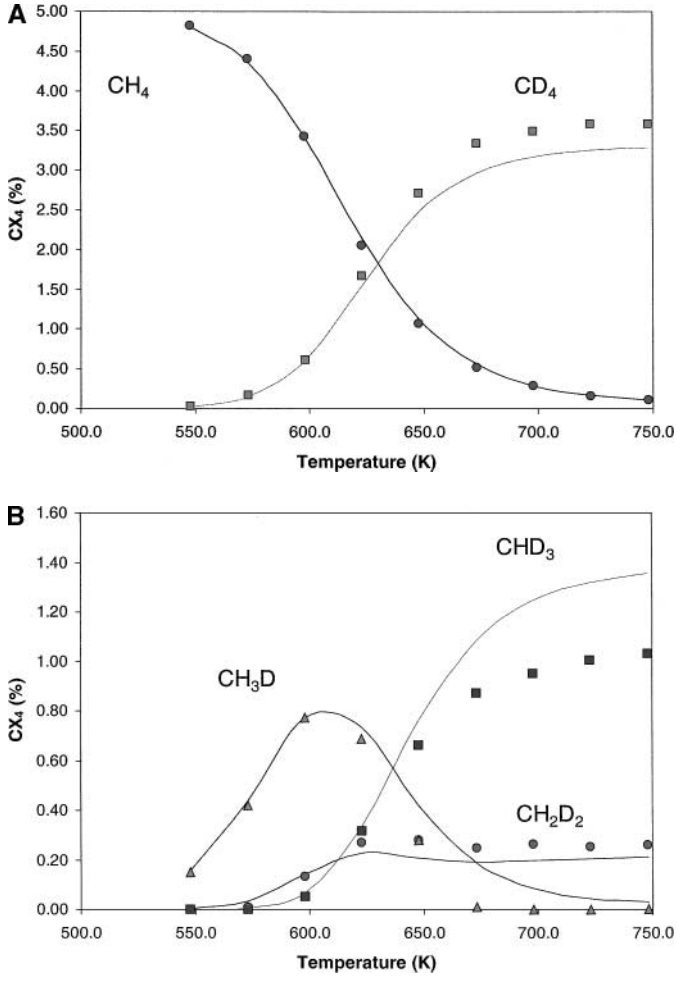

FIG. 11. Steady state concentrations of CH_4 and CD_4 (A) and CH_3D, CH_2D_2, and CHD_3 (B) out of the reactor as determined by the spectrometer signals at mass 16–20 for the $Ni/MgAl_2O_4$ catalyst. The full line curves are the results of microkinetic modeling.

$$CX_2* + * \rightleftharpoons CX* + X* \qquad [3]$$

$$k_3 = 1.4 \times 10^{13} \left(\frac{\text{molec}}{\text{site} \cdot \text{s}}\right) \exp\left(\frac{-28\ \text{kJ/mol}}{\text{RT}}\right),$$

$$k_{-3} = 3.7 \times 10^{12} \left(\frac{\text{molec}}{\text{site} \cdot \text{s}}\right) \exp\left(\frac{-75.5\ \text{kJ/mol}}{\text{RT}}\right),$$

$$X_2 + 2* \rightleftharpoons 2X* \qquad [4]$$

$$k_4 = 2 \times 10^{8} \left(\frac{\text{molec}}{\text{site} \cdot \text{bar} \cdot \text{s}}\right) \exp\left(\frac{-5\ \text{kJ/mol}}{\text{RT}}\right),$$

$$k_{-4} = 10^{13} \left(\frac{\text{molec}}{\text{site} \cdot \text{s}}\right) \exp\left(\frac{-91\ \text{kJ/mol}}{\text{RT}}\right).$$

In the reactions above, X is either H or D, k_n and k_{-n} are rate constants in the forward and reverse directions, and $*$ is an active nickel site. The model assumes that the reactions are reversible, ignores kinetic isotope effects, and expresses

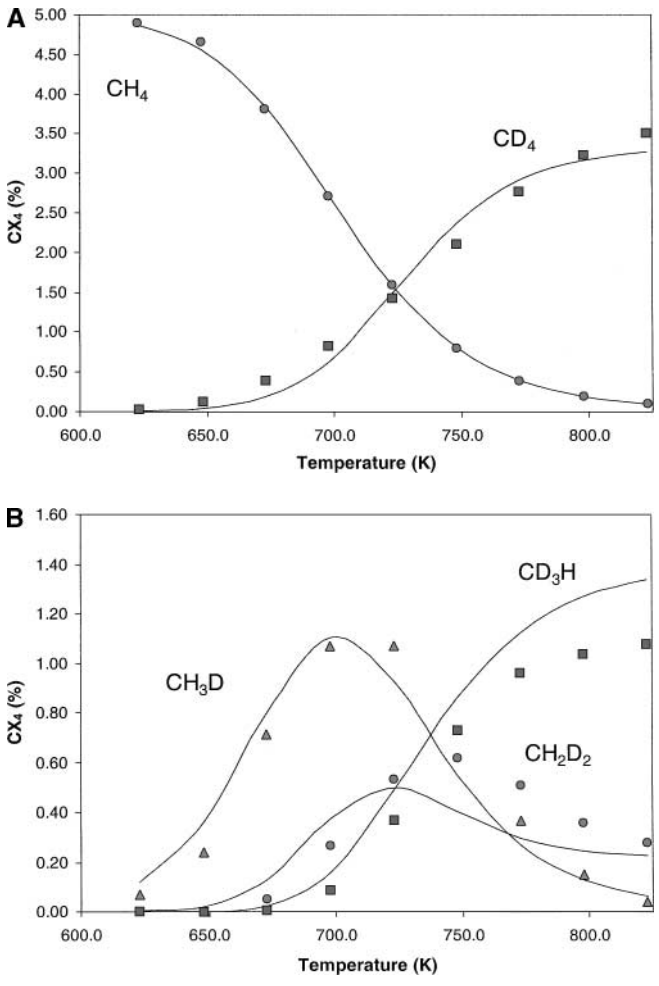

FIG. 12. Steady state concentrations of CH_4 and CD_4 (A) and CH_3D, CH_2D_2, and CHD_3 (B) out of the reactor as determined by the spectrometer signals at mass 16–20 for the $K/Ni/MgAl_2O_4$ catalyst. The full line curves are the results of microkinetic modeling.

each rate constant as the product of a preexponential factor times an exponential term containing an activation energy. The absence of an elementary reaction leading to adsorbed carbon, C∗, in the scheme, such as

$$CX* + * \rightleftharpoons C* + X* \quad k_5, k_{-5}, \qquad [5]$$

does not imply the absence of such a reaction. However, the experimental results could only be modeled when it was assumed that the H : D ratio in the $*CX_2$ species is the same as the H : D ratio in the hydrogen/deuterium gas over the catalyst. This implies that the rates of reactions [3], [4], and [−4] are fast compared to reaction [−2]. This is in complete agreement with the DFT results shown in Fig. 1.

Four parameters were adjusted to fit the model to the experimental data. They were the two parameters describing the rate constants of reaction [1] and the ratio of the preexponential factors of reactions [−1] and [2], A_{-1}/A_2, and the difference between the activation energies for these two reactions, $E_{-1} - E_2$. All other parameters were estimated a priori.

The parameters for the reverse rate constant of reaction [2] and the rate constants for reactions [3] and [−3] were obtained from Watwe *et al.* (27). Since the rate of reaction [3] is always much higher than that of reaction [2a] ($r_3/r_{-2} > 3300$) and $\theta_{CH_2} + \theta_{CH} \ll 1$ the choice of k_{-2}, k_3, and k_{-3} does not influence the four parameters determined from the data set.

The preexponential factor for reaction [−4] was assumed to be 10^{13} s^{-1}, as justified by transition state theory. The activation energy of reaction [−4] was determined from the modeling of the H_2 TPD spectra published by Christmann *et al.* (109) and Rendulic *et al.* (110). Using $A_{-4} = 10^{13}$ s^{-1} the activation energies of desorption of H_2 from Ni(111), Ni(100), Ni(110), and Ni(445) were determined to be 96, 90, 89, and 87 kJ/mol, respectively. In the following the average number of these values, $E_{-4} = 91$ kJ/mol, was used.

The forward preexponential factor for reaction [4] was calculated to be $2 \times 10^8 (\frac{\text{molec}}{\text{site} \cdot \text{bar}})$ by assuming a hydrogen sticking coefficient of 0.16 at a temperature of 623 K. Initial hydrogen sticking coefficients between 0.1 and 1 for nickel at gas temperatures between 373 and 1023 K or the equivalent molecular beam normal kinetic energy have been observed (110–114). The activation energy of adsorption, E_4, was determined by molecular beam experiments on Ni(111), Ni(100), Ni(110), and Ni(445) to be 9.6 (111), 5–5.9 (111, 115), 3.3 (111, 115), and 0 (110) kJ/mol, respectively. The activation energy of reaction [4] is assumed to be the average of these values: $E_4 = 5$ kJ/mol.

The procedure for fitting the model output to the experimental data was the following. First, the values of the preexponential factor and activation energy for reaction [1] were fitted to the temperature dependence of the CH_4 concentration. Second, the ratio of the preexponential factors of reactions [−1] and [2] and the difference between the activation energies for these reactions were fitted simultaneously to the temperature dependence of the other methane isotopomers.

The lines in Figs. 11 and 12 are results of the microkinetic modeling of the experimental data using the values given in Table 5. As seen from the figures the fit to the experimental data are good. Promoting with 1.2% potassium

TABLE 5

Parameters Obtained for the First Two Steps in the Dehydrogenation of Methane by Fitting the Experimental Data with a Microkinetic Model[a]

	A_1 (bar^{-1})	E_1 (kJ/mol)	A_{-1}/A_2	$E_{-1} - E_2$ (kJ/mol)
$Ni/MgAl_2O_4$	2×10^7	53.1	2.4×10^{-3}	−17.0
$K/Ni/MgAl_2O_4$	3×10^8	86.7	5.8×10^{-2}	−12.8

[a] See text for details.

dramatically reduces the activity for methane activation. An increase in the activation energy of 34 kJ/mol for sticking of methane upon promoting with 1.2% K is observed. Furthermore, the preexponential factor of reaction [1] increases by a factor of 15 by potassium promotion. These changes can be explained by the DFT calculations. DFT calculations show that potassium will block the step sites preferentially and that the activation energy is higher by 19 kJ/mol on Ni(111) (101 kJ/mol) compared to Ni(211) (82 kJ/mol), in good agreement with the increase in the activation energy observed here. The absolute magnitudes of the activation energies obtained from the microkinetic model and the DFT calculations are in good agreement when the zero-point correction is performed according to the model by Kratzer *et al.* (22). In addition, when potassium blocks the few very active step sites, which normally determine the activity of the catalyst, the less active sites on the nickel planes determine the overall activity of the catalyst. The increased number of active sites will give a higher preexponential factor. The methane activation experiments therefore strongly support the conclusions from the theoretical section.

8. CONCLUSIONS

The picture we arrive at is that both steam reforming and the nucleation of graphite over Ni catalysts is extremely structure sensitive. Certain step sites are considerably more reactive than close-packed facets for both reactions. We have also shown that the known promoters for this system, potassium, sulfur, and gold, preferentially bind to the step edges of Ni. We suggest that this is the main reason for the suppression of graphite formation observed for these systems.

When the step blocking additives are present the kinetics of the steam reforming process can change in two ways. If the additives block all step sites only the less reactive terraces are left. This will give rise to a different activation barrier and different reaction orders. The catalyst may however not have all step sites blocked. Many fewer sites need to be blocked in order to prevent nucleation of graphite at the step. In this case the steam reforming process may still proceed at the step sites that are left open, and the kinetics will only be changed in so far as the number of active sites has gone down. Complete blocking has been observed for methane activation experiments presented here, but the other situation is more likely for an optimally promoted catalyst. An optimized catalyst will have just enough additives that graphite formation is effectively blocked while the fast channel reaction can still proceed. This is in accordance with experimental evidence (60).

We also find that a certain minimum nucleus of graphene at a Ni step is needed before it is stable. The rate of graphite formation therefore involves the nucleation rate for these graphene islands growing out on the Ni(111) facets from step sites. Since the critical nucleus is quite large this is a slow process, in accordance with experimental evidence (1, 2, 106). If the facets or step edges are too small nucleation cannot proceed, and graphite formation is further suppressed. This explains why very small particles are found not to grow graphite under normal conditions. We also note that carbon is bound so strongly to steps that carbon can create new steps on an otherwise flat Ni(111) surface. The calculated step formation energy on Ni(111) is 16 kJ/mol/Ni step atom from this work, in reasonable agreement with the experimentally determined step formation energy extrapolated to 0 K of 9.8 kJ/mol/Å $\sim$ 24 kJ/mol/Ni step atom (116). The extra bonding for a full edge of adsorbed carbon relative to carbon on the terrace is 43 kJ/mol, showing that energy can be gained by forming new steps. We suggest that this effect explains the large rearrangements of particle morphology observed during graphite whisker growth (98).

In summary, we have shown that through a closely coupled theoretical and experimental approach, we have developed a consistent mechanism for the steam reforming process involving an atomistic description of all elementary steps in the process.

ACKNOWLEDGMENTS

We thank Lars B. Hansen for help with the DFT program and Lis Ibsen and Said Rokni for technical assistance with the TGA and the methane activation measurements. This work was supported by the Danish Research Councils through the Interdisciplinary Research Center for Catalysis (ICAT). The Center for Atomic-Scale Materials Physics (CAMP) is sponsored by the Danish National Research Foundation.

REFERENCES

1. Rostrup-Nielsen, J. R., *in* "Catalysis, Science and Technology," (J. R. Anderson and M. Boudart, Eds.), Vol. 5, Ch. 1, Springer-Verlag, Berlin, 1984.
2. Rostrup-Nielsen, J. R., "Steam Reforming Catalysts." Danish Technical Press, Copenhagen, 1975.
3. Rostrup-Nielsen, J. R., *J. Catal.* **85**, 31 (1984).
4. Besenbacher, F., Chorkendorff, I., Clausen, B. S., Hammer, B., Molenbroek, A. M., Nørskov, J. K., and Stensgaard, I., *Science* **279**, 1913 (1998).
5. Aparicio, L. M., *J. Catal.* **165**, 262 (1997).
6. Bradford, M. C. J., and Vannice, M. A., *Appl. Catal. A* **142**, 97 (1996).
7. Dahl, S., Logadottir, A., Egeberg, R. C., Larsen, J. H., Chorkendorff, I., Törnqvist, E., and Nørskov, J. K., *Phys. Rev. Lett.* **83**, 1814 (1999).
8. Zambelli, T., Wintterlin, J., Trost, J., and Ertl, G., *Science* **273**, 1688 (1996).
9. Kratzer, P., Pehlke, E., Scheffler, M., Raschke, M. B., and Höfer, U., *Phys. Rev. Lett.* **81**, 5596 (1998).
10. Perdew, J. P., Chevary, J. A., Vosko, S. H., Jackson, K. A., Pederson, M. R., Singh, D. J., and Fiolhais, C., *Phys. Rev. B* **46**, 6671 (1992).
11. Hammer, B., Hansen, L. B., and Nørskov, J. K., *Phys. Rev. B* **59**, 7413 (1999).
12. Kresse, G., and Furthmüller, J., *Comput. Mater. Sci.* **6**, 15 (1996).
13. Kurth, S., Perdew, J. P., and Blaha, P., *Int. J. Quantum Chem.* **75**, 889 (1999).
14. Hammer, B., *J. Catal.* **199**, 171 (2001).

15. Mills, G., Jónsson, H., and Schenter, G., *Surf. Sci.* **324**, 305 (1995).
16. Jónsson, H., Mills, G., and Jacobsen, K. W., *in* "Classical and Quantum Dynamics in Condensed Phase Simulations" (B. J. Berne, G. Ciccotti, and D. F. Coker, Eds.). World Scientific, Singapore, Ch. 16, 1997.
17. Burghgraef, H., Jansen, A. P. J., and van Santen, R. A., *Surf. Sci.* **324**, 345 (1995).
18. Burghgraef, H., Jansen, A. P. J., and van Santen, R. A., *J. Chem. Phys*. **101**, 11012 (1994).
19. Yang, H., and Whitten, J. L., *Surf. Sci.* **255**, 193 (1991).
20. Yang, H., and Whitten, J. L., *J. Chem. Phys*. **96**, 5529 (1992).
21. Siegbahn, P. E. M., and Panas, I., *Surf. Sci.* **240**, 37 (1990).
22. Kratzer, P., Hammer, B., and Nørskov, J. K., *J. Chem. Phys*. **105**, 5595 (1996).
23. Au, C.-T., Liao, M.-S., and Ng, C.-F., *J. Phys. Chem. A* **102**, 3959 (1998).
24. Au, C.-T., Ng, C.-F., and Liao, M.-S., *J. Catal*. **185**, 12 (1999).
25. Michaelides, A., and Hu, P., *J. Chem. Phys*. **112**, 6006 (2000).
26. Michaelides, A., and Hu, P., *J. Chem. Phys*. **112**, 8120 (2000).
27. Watwe, R. M., Bengaard, H. S., Rostrup-Nielsen, J. R., Dumesic, J. A., and Nørskov, J. K., *J. Catal*. **189**, 16 (2000).
28. Ciobîcă, I. M., Frechard, F., van Santen, R. A., Kleyn, A. W., and Hafner, J., *Chem. Phys. Lett*. **311**, 185 (1999).
29. Ciobîcă, I. M., Frechard, F., van Santen, R. A., Kleyn, A. W., and Hafner, J., *J. Phys. Chem. B* **104**, 3364 (2000).
30. Paul, J.-F., and Sautet, P., *Stud. Surf. Sci. Catal*. **101**, 253 (1996).
31. Paul, J.-F., and Sautet, P., *J. Phys. Chem. B* **102**, 1578 (1998).
32. Henkelman, G., and Jonsson, H., *Phys. Rev. Lett.* **86**, 664 (2001).
33. Beebe, T. P., Jr., Goodman, D. W., Kay, B. D., and Yates, J. T., Jr., *J. Chem. Phys*. **87**, 2305 (1987).
34. Chorkendorff, I., Alstrup, I., and Ullmann, S., *Surf. Sci.* **227**, 291 (1990).
35. Nielsen, B. Ø., Luntz, A. C., Holmblad, P. M., and Chorkendorff, I., *Catal. Lett.* **32**, 15 (1995).
36. Larsen, J. H., and Chorkendorff, I., *Surf. Sci. Rep*. **35**, 163 (1999).
37. Lee, M. B., Yang, Q. Y., Tang, S. L., and Ceyer, S. T., *J. Chem. Phys*. **85**, 1693 (1986).
38. Yang, Q. Y., Maynard, K. J., Johnson, A. D., and Ceyer, S. T., *J. Chem. Phys*. **102**, 7734 (1995).
39. Bengaard, H. S., and Nørskov, J. K., manuscript in preparation.
40. Christoffersen, E., Stoltze, P., and Nørskov, J. K., manuscript in preparation.
41. Brodén, G., Rhodin, T. N., and Brucker, C., *Surf. Sci.* **59**, 593 (1976).
42. Nakano, H., Kawakami, S., Fujitani, T., and Nakamura, J., *Surf. Sci.* **454–456**, 295 (2000).
43. Erley, W., and Wagner, H., *Surf. Sci.* **74**, 333 (1978).
44. Steinrück, H. P., D'Evelyn, M. P., and Madix, R. J., *Surf. Sci.* **172**, L561 (1986).
45. Rosei, R., Ciccacci, F., Memeo, R., Mariani, C., Caputi, L. S., and Papagno, L., *J. Catal*. **83**, 19 (1983).
46. Astaldi, C., Santoni, A., Della Valle F., and Rosei, R., *Surf. Sci.* **220**, 322 (1989).
47. Kasza, R. V., Griffiths, K., Shapter, J. G., Norton, P. R., and Harrington, D. A., *Surf. Sci.* **356**, 195 (1996).
48. Benndorf, C., and Mundt, C., *J. Vac. Sci. Technol. A* **10**, 3026 (1992).
49. Mundt, C., and Benndorf, C., *Surf. Sci.* **287/288**, 119 (1993).
50. Mundt, C., and Benndorf, C., *Surf. Sci.* **307–309**, 28 (1994).
51. Hoffmann, W., and Benndorf, C., *J. Vac. Sci. Technol. A* **18**, 1520 (2000).
52. Koper, M. T. M., and van Santen, R. A., *J. Electroanal. Chem*. **472**, 126 (1999).
53. Yang, H., and Whitten, J. L., *Surf. Sci.* **370**, 136 (1997).
54. Pedio, M., Becker, L., Hillert, B., D'Addato, S., and Haase, J., *Phys. Rev. B* **41**, 7462 (1990).
55. Caputi, L. S., Jiang, S. L., Amoddeo, A., and Tucci, R., *Phys. Rev. B* **41**, 8513 (1990).
56. Kirstein, W., Petraki, I., and Thieme, F., *Surf. Sci.* **331**, 162 (1995).
57. Gray, D. E., Ed., "American Institute of Physics Handbook." McGraw–Hill, New York, 1972.
58. Weast, R. C., Ed., "CRC Handbook of Chemistry and Physics." CRC Press, Boca Raton, FL, 1983.
59. For a review, see, e.g., Bonzel, H. P., Bradshaw, A. M., and Ertl, G., Eds., "Physics and Chemistry of Alkali Metal Adsorption." Elsevier, Amsterdam/New York, 1989.
60. Rostrup-Nielsen, J. R., and Christiansen, L. J., *Appl. Catal. A* **126**, 381 (1995).
61. Ceyer, S. T., Yang, Q. Y., Lee, M. B., Beckerle, J. D., and Johnson, A. D., *Stud. Surf. Sci. Catal.* **36**, 51 (1988).
62. Bengaard, H. S., Alstrup, I., Chorkendorff, I., Ullmann, S., Rostrup-Nielsen, J. R., and Nørskov, J. K., *J. Catal*. **187**, 238 (1999).
63. Huang, Z., Wang, L. Q., von Wittenau, A. E. S., Hussain, Z., and Shirley, D. A., *Phys. Rev. B* **47**, 13626 (1993).
64. Davis, R., Hu, X.-M., Woodruff, D. P., Weiss, K.-U., Dippel, R., Schindler, K.-M., Hoffmann, Ph., Fritzsche, V., and Bradshaw, A. M., *Surf. Sci.* **307–309**, 632 (1994).
65. Kaukasoina, P., Lindroos, M., Diehl, R. D., Fisher, D., Chandavarkar, S., and Collins, I. R., *J. Phys. Condens. Matter* **5**, 2875 (1993).
66. Garfunkel, E. L., and Somorjai, G. A., *Surf. Sci.* **115**, 441 (1982).
67. Albano, E. V., *Surf. Sci.* **215**, 333 (1989).
68. Diehl, R. D., and McGrath, R., *Surf. Rev. Lett*. **2**, 387 (1995).
69. Li, Z. Y., and Diehl, R. D., *J. Phys. Condens. Matter* **9**, 3701 (1997).
70. Murray, S. J., Brooks, D. A., Leibsle, F. M., Diehl, R. D., and McGrath, R., *Surf. Sci.* **314**, 307 (1994).
71. Finetti, P., Leatherman, G. S., Caragiu, M., Lindroos, M., McGrath, R., and Diehl, R. D., *Surf. Sci.* **462**, 77 (2000).
72. Finetti, P., Murray, S. J., Mercer, J., Johal, T. K., Robinson, A. W., Dhanak, V. R., and McGrath, R., *Surf. Rev. Lett*. **4**, 1341 (1997).
73. Van Hardeveld, R., and Van Montfoot, A., *Surf. Sci.* **4**, 396 (1966).
74. Van Hardeveld, R., and Hartog, F., *Surf. Sci.* **15**, 189 (1969).
75. Van Hardeveld, R., and Van Montfoot, A., *Surf. Sci.* **17**, 90 (1969).
76. Nieuwenhuys, B. E., and Sachtler, W. M. H., *J. Colloid Interface Sci*. **58**, 66 (1977).
77. Shigeishi, R. A., and King, D. A., *Surf. Sci.* **62**, 379 (1977).
78. Quick, A., Browne, V. M., Fox, S. G., and Hollins, P., *Surf. Sci.* **221**, 48 (1989).
79. Yoshinobu, J., Zenobi, R., Xu, J., and Yates, J. T., *J. Chem. Phys*. **95**, 9393 (1991).
80. Arumainayagam, C. R., Tripa, C. E., Xu, J., and Yates, J. T., *Surf. Sci.* **360**, 121 (1996).
81. Tripa, C. E., Zubkov, T. S., Yates, J. T., Mavrikakis, M., and Nørskov, J. K., *J. Chem. Phys*. **111**, 8651 (1999).
82. Horn, K., DiNardo, J., Eberhardt, W., Freund, H.-J., and Plummer, E. W., *Surf. Sci.* **118**, 465 (1982).
83. Perdereau, M., and Oudar, J., *Surf. Sci.* **20**, 80 (1970).
84. Lüdecke, J., Ettema, A. R. H. F., Driver, S. M., Scragg, G., Kerkar, M., Woodruff, D. P., Cowie, B. C. C., Jones, R. G., and Bastow, S., *Surf. Sci.* **366**, 260 (1996).
85. Ku, Y.-S., and Overbury, S. H., *Surf. Sci.* **276**, 262 (1992).
86. Demuth, J. E., Jepsen, D. W., and Marcus, P. M., *Phys. Rev. Lett.* **32**, 1182 (1974).
87. Warburton, D. R., Wincott, P. L., Thornton, G., Wuinn, F. M., and Norman, D., *Surf. Sci.* **211/212**, 71 (1989).
88. Edmonds, T., McCarroll, J. J., and Pitkethly, R. C., *J. Vac. Sci. Technol*. **8**, 68 (1971).
89. Woodruff, D. P., *J. Phys. Condens. Matter* **6**, 6067 (1994).
90. Maurice, V., Kitakatsu, N., Siegers, M., and Marcus, P., *Surf. Sci.* **373**, 307 (1997).
91. Fauster, Th., Dürr, H., and Hartwig, D., *Surf. Sci.* **178**, 657 (1986).
92. Jacobsen, K. W., Nørskov, J. K., and Puska, M. J., *Phys. Rev. B* **35**, 7423 (1987).

93. Stoltze, P., "Simulation Methods in Atomic-Scale Materials Physics." Polyteknisk Forlag, Lyngby, Denmark, 1997.
94. Hansen, P. L., Molenbroek, A. M., and Ruban, A. V., *J. Phys. Chem. B* **101**, 1861 (1997).
95. Molenbroek, A. M., Nørskov, J. K., and Clausen, B. S., *J. Phys. Chem. B* **105**, 5450 (2001).
96. Rehr, J. J., Mustre de Leon, J., Zabinsky, S. I., and Albers, R. C., *J. Am. Chem. Soc.* **113**, 5135 (1991).
97. Ankudinov, A. L., Ravel, B., and Rehr, J. J., *Phys. Rev. B* **58**, 7565 (1998).
98. Alstrup, I., *J. Catal.* **1**, 241 (1988).
99. Alstrup, I., Tavares, M. T., Bernardo, C. A., Sørensen, O., and Rostrup-Nielsen, J. R., *Mater. Corr.* **49**, 367 (1998).
100. Holstein, W. L., *J. Catal.* **152**, 42 (1995).
101. Rostrup-Nielsen, J. R., and Trimm, D. L., *J. Catal.* **48**, 155 (1977).
102. Gamo, Y., Nagashima, A., Wakabayashi, M., Terai, M., and Oshima, C., *Surf. Sci.* **374**, 61 (1997).
103. Lee, Y. H., Kim, S. G., and Tomanek, D., *Phys. Rev. Lett.* **78**, 2393 (1997).
104. Wu, M.-C., Xu, Q., and Goodman, D. W., *J. Phys. Chem.* **98**, 5104 (1994).
105. Grenga, H. E., and Lawless, K. R., *J. Appl. Phys.* **43**, 1508 (1972).
106. Snoeck, J.-W., Froment, G. F., and Fowles, M., *J. Catal.* **169**, 240 (1997).
107. Borowiecki, T., *Appl. Catal.* **4**, 223 (1982).
108. Dumesic, J. A., Rudd, D. F., Aparicio, L. M., Rokoske, J. E., and Treviño, A. A., "The Microkinetics of Heterogeneous Catalysis." Am. Chem. Soc., Washington, DC, 1993.
109. Christmann, K., Schober, O., Ertl, G., and Neumann, M., *J. Chem. Phys.* **69**, 4528 (1974).
110. Rendulic, K. D., Winkler, A., and Steinrück, H. P., *Surf. Sci.* **185**, 469 (1987).
111. Rendulic, K. D., Winkler, A., and Karner, H., *J. Vac. Sci. Technol. A* **5**, 488 (1987).
112. Steinrück, H. P., Rendulic, K. D., and Winkler, A., *Surf. Sci.* **154**, 99 (1985).
113. Winkler, A., and Rendulic, K. D., *Surf. Sci.* **118**, 19 (1982).
114. Rendulic, K. D., Anger, G., and Winkler, A., *Surf. Sci.* **208**, 404 (1989).
115. Hamza, A. V., and Madix, R. J., *J. Phys. Chem.* **89**, 5381 (1985).
116. Bonzel, H. P., *Surf. Sci.* **328**, L571 (1995).